Spectrally Dependent CLARREO Infrared Spectrometer Calibration Requirement for Climate Change Detection

Xu Liu*

NASA Langley Research Center, Hampton, Virginia

Wan Wu

Science Systems and Applications Inc, Hampton, Virginia

Bruce. A. Wielicki

NASA Langley Research Center, Hampton, Virginia

Qiguang Yang, Susan H. Kizer

Science Systems and Applications Inc, Hampton, Virginia

Xianglei Huang, Xiuhong Chen

Department of Climate and Space Science and Engineering,

University of Michigan, Ann, Arbor, Michigan

Seiji Kato, Yolanda. L. Shea, and Martin G. Mlynczak

NASA Langley Research Center, Hampton, Virginia

ABSTRACT

Detecting climate trends of atmospheric temperature, moisture, cloud, and surface temperature requires accurately calibrated satellite instruments such as the Climate Absolute Radiance and Reflectivity Observatory (CLARREO). Wielicki et al. have studied the CLARREO measurement requirements for achieving climate change accuracy goals in orbit. Our study further quantifies the spectrally dependent IR instrument calibration requirement for detecting trends of atmospheric temperature and moisture profiles. The temperature, water vapor, and surface skin temperature variability and the associated correlation time are derived using Modern Era Retrospective-Analysis for Research and Applications (MERRA) and European Center for Medium-Range Weather Forecasts (ECMWF) reanalysis data. The results are further validated using climate model simulation results. With the derived natural variability as the reference, the calibration requirement is established by carrying out a simulation study for CLARREO observations of various atmospheric states under all-sky. We derive a 0.04 K (*k*=2, or 95% confidence) radiometric calibration requirement baseline using a spectral fingerprinting method. We also demonstrate that the requirement is spectrally dependent and some spectral regions can be relaxed due to the hyperspectral nature of the CLARREO instrument. We further discuss relaxing the requirement to 0.06 K (*k*=2) based on the uncertainties associated with the temperature and water vapor natural variability and relatively small delay in time-to-detect for trends relative to the baseline case. The methodology used in this study can be extended to other parameters (such as clouds and CO_2) and other instrument configurations.

1. Introduction

The CLARREO mission has been proposed to provide the essential observations for climate change on decadal timescales with high accuracy that are traceable to International System of Units (SI) standards. The demand for high absolute calibration accuracy of the CLARREO instrument is driven by the need to accurately determine the climate trend with minimum time delay relative to a perfect observation system (Wielicki et al. 2013) and by the need to accurately calibrate other satellite instruments so that data such as those from operational weather sounders and from the Earth energy budget instruments can be used to improve climate change detection.

To detect an accurate trend for a geophysical parameter, the observation system has to be able to separate the natural variability from anthropogenic climate changes. Therefore, even for a perfect observation system, one has to make sufficiently long observations to minimize the contribution from the natural variability. For a perfect observation system, the trend uncertainty for a selected geophysical parameter is statistically determined by its variability, $\sigma_{var,}$, and autocorrelation time, τ_{var}, as has been explained in both Weatherhead's (Weatherhead et al. 1998) and Leroy's (Leroy et al. 2008a) papers. How the measurement uncertainty affects the trend detection uncertainty is quantified by the accuracy uncertainty factor U_a (Wielicki et al. 2013), where U_a is given as

$$U_a = \sqrt{1 + (\sigma_{cal}^2 \tau_{cal} + \sigma_{instru}^2 \tau_{instru} + \sigma_{orbit}^2 \tau_{orbit})/(\sigma_{var}^2 \tau_{var})} \qquad (1)$$

U_a defines the ratio of the trend detection uncertainty of a real system over that of a perfect system. The measurement uncertainty includes the calibration, σ_{cal}, instrument noise,

σ_{instru}, and orbit sampling error, σ_{orbit}, uncertainties, with their associated autocorrelation times, τ_{cal}, τ_{instru}, and τ_{orbit}. We can derive the calibration requirement to be

$$\sigma_{cal} = \sqrt{\frac{(U_a^2-1)\sigma_{var}^2\tau_{var} - \sigma_{instru}^2\tau_{instru} - \sigma_{orbit}^2\tau_{orbit}}{\tau_{cal}}} \qquad (2)$$

In this paper, we assume that calibration uncertainty is the dominant factor of the total measurement uncertainty. Other factors such as the uncertainty due to instrument random noise can be minimized by performing spatial and temporal averaging of the observed spectra. Wielicki et al. (2013) have concluded that the orbital sampling error is small compared to natural variability even with just one 90^{o} orbit. Eq. (2) can be further simplified as

$$\sigma_{cal} = \sqrt{\frac{(U_a^2-1)\tau_{var}}{\tau_{cal}}}\ \sigma_{var} \qquad (3)$$

where σ_{cal} is the observation accuracy for a geophysical parameter that can be achieved assuming some value for the trend detection uncertainty factor, U_a. It should be noted here that the calibration requirement, σ_{cal}, defined in Eq. (2) and Eq. (3) is not the direct spectral calibration requirement imposed on the instrument. It is the observation accuracy uncertainty of geophysical parameters that are essential to climate change study. To obtain the spectral calibration requirement for the Fourier Transform based IR instrument of CLARREO, the inverse relationship between the spectral calibration error and the associated error for the geophysical variables needs to be established. The attribution of the change in the measured IR spectra to climate change signals (i.e. changes in temperature, water vapor, cloud property, surface property, etc.) has been studied using spectral fingerprinting methods (Leroy et al. 2008b, Huang et al. 2010, and Kato et al. 2011). We use a similar method to perform the inversion of radiance change to the geophysical parameter change. Our goal is to characterize a spectrally dependent instrument calibration requirement so that we can accurately detect the atmospheric temperature and moisture profile changes within the uncertainties defined by σ_{cal}.

The nominal design of the IR spectrometer of CLARREO has a 0.5 cm^{-1} spectral resolution with a spectral coverage from 200 to 2000 cm^{-1}. The additional spectral coverage of the Far-IR from 200 to 645 cm^{-1} , which is not currently included in hyperspectral sounders such as the Cross-track Infrared Sounder (CrIS), the Atmospheric Infrared Sounder (AIRS), and the Infrared Atmospheric Sounding Interferometer (IASI), will allow the CLARREO instrument to measure nearly half of the outgoing longwave radiation currently unobserved by current sounders and will provide additional information on cirrus clouds and upper tropospheric water vapor. The CO_2 atmospheric emission lines with various transmittances will provide vertical temperature profile information. The H_2O emission lines will provide vertical water vapor vertical profile information. The window spectral regions will provide information on surface skin temperature and surface emissivity. The broad spectral coverage will enable the CLARREO instrument to characterize cloud top height, cloud phase, cloud amount, and cloud particle size.

Due to the hyperspectral nature of the IR instrument, information from one channel may be highly correlated with others. For example, the CO_2 $v2$ perpendicular vibrational band near 15 μm has P, Q, and R branches. The R-branch, which is located on the shorter wavelength side of the Q-branch, has similar information content as the P-branch, which is on the longer wavelength side of the Q-branch. We can tolerate larger calibration errors for those channels in the CO_2 P-branch as long as we can accurately calibrate the spectral region that covers the R-branch (or vice versa). Based on this rationale, we may be able to relax the calibration requirement for spectral regions where the transmittances of the FTS optics or the detector sensitivities are low (e.g., at spectral band edges).

The details of this study is conatained in Sections 2 and 3. Section 2 of this paper describes the efforts to derive natural variability values using de-seasonalized MERRA (Rienecker at al. 2011) and ECMWF ERA-Interim (Dee et al. 2011) data, which include the information from multiple decades of satellite data. Our approach follows the trend analysis methodology of Weatherhead et al. (Weatherhead et al. 1998) and Leroy et al. (Leroy et al. 2008a). Both methods assume the representation of climate anomalies in a time series using a linear trend model with noise processes (natural variability) embedded and correlated among successive measurements. Climate anomalies here can be viewed as a linear combination of the climate trends (a_o in Equation 5), the climate variations associated with known climate forcing factors, and the natural variability,

$$Y(t) = a_0 t + C(t) + \varepsilon, \tag{5}$$

where Y is the climate anomalies as a function of time t, C is the contribution of climate forcing factors and ε is the natural variability. The effects of major climate forcing factors including volcanic eruptions, solar cycle forcing, El Niño-Southern Oscillation (ENSO) variability, and the quasi-biennial oscillation (QBO) in the time series data have been accounted for in our linear regression analysis. Although ENSO and QBO are classified as ‘internal’ forcing factors, the success of including them in the climate model simulations (Philander, et.al. 1992; Takahashi, 1999) proves the feasibility of separating them from other uncharacterized natural variations. If the response of the climate variation to major climate forcing factors can be reliably estimated using representative indices (to be discussed in Section 2), removing these climate signals from the anomalies will greatly facilitate the linear trend analysis by reducing the uncertainties caused by the naturally occurring variations. Other contributors to natural variability including Pacific Decadal Oscillation (PDO) and Atlantic Meridional Overturning Circulation (AMOC) are not included in this analysis due to their insignificant impact within a decadal scale as compared with ENSO. Our goal in this paper is not to derive an accurate climate trend, but rather to systematically characterize the temperature and water vapor anomalies in order to derive the magnitude of natural variability at all significant atmospheric altitudes. Our results obtained from one set of reanalysis data (e.g. MERRA) can be validated using the results from the other reanalysis data set (e.g. ECMWF).

In addition to the comparison study between results from the MERRA data and those from ECMWF data, we further compare the reanalysis results with those from a General Circulation Model (GCM) simulation made by the NOAA Geophysical Fluid Dynamics Laboratory (GFDL) for the Coupled Model Intercomparison Project Phase 5 (CMIP5). Natural variability for the vertical profile of temperature and moisture and the surface skin temperature are calculated and presented. Our goal is to derive reliable natural variability values, σ_{var}, that can be used to define the calibration requirement, σ_{cal}.

Section 3 discusses the simulation study to establish the baseline for the spectral calibration requirement and how the requirements for specific channels are modified to accommodate the instrumentation concerns. We summarize the information content difference between channels in various wavelength regions and illustrate how σ_{cal} changes in correspondence to the change in spectral calibration errors. Limiting factors that determine the calibration requirement are discussed. We then present feasible spectral calibration requirement solutions that take potential engineering concerns into consideration. In Section 3, we also discuss the impact of calibration errors on the time to detect climate trends and how the CLARREO IR can be used in synergy with current and future operational sounders to decrease the time needed to detect the temperature climate trends accurately. Fig. 1 shows a flowchart summarizing the procedures used in Sections 2 and 3 to derive the instrument calibration requirement.

Finally, we present our conclusions on the methodology developed in this study and how we can improve the work in future studies.

2. Natural variability study

Continuous time series for temperature, water vapor and surface skin temperature are obtained from MERRA and ERA-interim data. Both time series data sets consist of monthly mean results of the satellite observation era (from January 1979 to December 2013). The MERRA data are obtained from Goddard Earth Sciences Data and Information Service Center as daily means for $1.25^{o}\times1.25^{o}$ latitude/longitude grid boxes. The monthly mean values are derived from the daily means. The ECMWF data are available as monthly means for $3^{o}\times3^{o}$ latitude/longitude grid boxes. Global mean or zonal mean values are calculated as the weighted average of all the non-missing, grid-box values. The weights used are the cosines of the central latitudes of each grid box. Anomalies are calculated using the de-seasonalized global mean time series data by subtracting the monthly mean data in all years from each individual monthly data value. Both temperature and water vapor data of MERRA and ECMWF are collected as vertical profile layer quantities on pressure grids extending from 1000 hPa to 1 hPa. Both pressure grids are divided into 37 levels, although their pressure level values are not identical. Atmospheric temperature and water vapor variability are obtained by applying trend analyses on the time series anomalies for each layer and estimating the standard errors.

The pre-industrial control run (piControl) from the GFDL CM3 model (Donner et al., 2011) is also used in this study. Global mean values are again calculated as the weighted average of all the grid-box values with a $2^{o} \times 1.5^{o}$ latitude/longitude spatial resolution and a 23-layer pressure grid (1 hPa ~ 1000 hPa). We apply a similar procedure as mentioned in the previous paragraph to de-seasonalize the time series data and extract trend and natural variability out of the de-seasonalized data.

a. Temperature

Major climate forcing factors that have been taken into consideration for the global temperature trend study generally consist of ‘external forcings’ which include short-term volcanic eruption and solar variability and ‘internal variability’ which includes ENSO and QBO. The relative influence of each climate forcing factor can be estimated by performing multiple regression of temperature against their proxy data. By removing contributions from these factors, a linear trend, which represents the climate change due to anthropogenic factors, can then be derived. Previous climate trend studies have focused on the impact of the above known factors on temperature variations in different atmospheric regions. Effects of ENSO and volcanoes on the global surface temperature trend were illustrated in various papers (Wigley et al. 2000, Lean et al. 2008, Foster et al. 2011). Angell et al. (2000) studied the influence of ENSO in tropospheric temperature variations. Santer et al. (2001) accounted for the effects of both volcanoes and ENSO in tropospheric temperature trends. The influence of solar activity on surface temperature was addressed by both Lean and

Foster (Lean et al. 2008, Foster et al. 2011). Crooks et al. (2005) used an ECMWF dataset of the period 1979-2001 to study the influence of the 11-year solar cycle on atmospheric temperature and zonal winds with volcanic, ENSO, and quasi-biennial oscillation (QBO) signatures being extracted as part of the multivariate regression analysis. Chiodo et al. (2014) investigated the relative role of volcanic eruptions, ENSO, and QBO in the quasi-decadal signal in the tropical stratosphere with regard to temperature and ozone attributed to the 11-year solar cycle. Although the QBO's signature in the low troposphere to surface region has been neglected in the papers as mentioned above, Powell et al. (2013) showed the globally distributed response of tropospheric temperature to the QBO, and that the most of the statistically significant area was over the mid-high latitudes.

ENSO is usually characterized by the southern oscillation index (SOI) (Wigley et al. 2000, Santer et al. 2001), the multivariate ENSO index (MEI) (Lean et al. 2008, Foster et al. 2011), or sea surface temperatures for the Niño3 and 3.4 regions (Angell et al. 2000, Santer et al. 2001). Solar influence can be characterized using monthly sun spot numbers (Foster et al. 2011), the solar 10.7-cm radio flux (Crooks et al. 2005, Powell et al. 2013), ultraviolet solar radiation flux integrated in the Hartley band (240–270 nm) (Chiodo et al. 2014), or total solar irradiance (Lean et al. 2008, Foster et al. 2011). The choice of QBO proxy indices include zonal wind time series at 30 and 10 hPa (Chiodo et al. 2014, Powell et al. 2013) or principal components of averaged stratospheric zonal wind indices (Crooks et al. 2005). The volcanic aerosol effect has been estimated using global stratospheric aerosol optical depth (AOD) (Foster et al. 2011, Powell et al. 2013, Crooks et al. 2005). Our multiple-regression experiments show that the choice of characteristic proxy for climate forcing factors in general is believed to have an insignificant effect on the trend analysis and the uncertainty of a certain climate forcing signal due to the inaccuracy of the proxy indices has negligible impact on the analysis for other climate forcing signals.

We choose MEI from the NOAA MEI website to characterize ENSO. The multivariate ENSO index, which is derived from sea-level pressure, sea surface wind, sea surface temperature, air temperature, and cloud fraction, provides a more complete and flexible description of the nature of the coupled ocean-atmosphere system and is less vulnerable to occasional data glitches in the monthly update cycles and thus more suitable for the global ENSO impact study (Wolter et al., 2011). We use zonal average of the 30 hPa zonal wind at the equator as the QBO index, and monthly sun spot numbers are used as a proxy for solar activity. We characterize volcanic influence by the AOD data from the NASA Goddard Institute for Space Studies website, which are derived from optical extinction data (Sato et al. 1993).

Considering the delayed response of temperature anomaly to the climate forcing factors, the multiple regression analysis is carried out with optimally lagged climate forcing signals and the naturally occurring temperature, ε, is given as

$$\varepsilon = T(t) - a_0 t - a_1 E(t - \tau_1) - a_2 Q(t + \tau_2) - a_3 S(t + \tau_3) - a_4 V(t + \tau_4) \qquad (6)$$

where $T(t)$ is the temperature anomaly and $E(t)$, $Q(t)$, $S(t)$, and V(t) are MEI, QBO index, Sun spot number, and AOD in time series. We carry out the lag-correlation analysis using values from 0 to 24 months for each of the four factors, and then select the lag values (τ_1, τ_2, τ_3, τ_4) that correspond to the best fit. Once the lag values are obtained a multiple regression is performed to obtain the ε(t) with climate trend (a_o) and other factors removed. Fig. 2 and Fig. 3 are examples that demonstrate the influence of climate forcing factors on global temperature data from MERRA and ECMWF at 70 hPa and 975 hPa. Those two figures clearly illustrate the difference between the climate forcing signature in the stratosphere and that in the troposphere. Generally speaking, volcanic aerosol induces strong heating in the stratosphere and cooling in the troposphere. Solar activity influence is much stronger in the stratosphere as compared with its influence in the troposphere, while ENSO influence is stronger in the troposphere. Fig. 4 illustrates the influence of different forcing factors on the global surface skin temperature trend. The multiple regression analysis gives similar results for both MERRA and ECMWF temperature records. Both results demonstrate a cooling temperature trend at 70 hPa and a warming trend in lower tropospheric and surface temperature. With the attribution of different climate forcings fully accounted for, naturally occurring variations of temperature at specific altitudes can then be estimated and validated with the climate model simulation results.

Fig. 5 compares the temperature variability from reanalysis data with that from the 35-year-long GFDL CM3 model piControl output. The CMIP5 piControl experiment with CM3 imposes non-evolving, pre-industrial conditions that do not include volcanic eruption influences and assumes constant solar forcing (Taylor et al., 2009). The difference between tropospheric temperature variation from MERRA, ECMWF and the GFDL CM3 model is smaller than 0.05 K after we subtract those two external forcing influences from the reanalysis temperature anomaly data. The discrepancy among the three sets of results is much larger at high altitude, starting from the tropopause (located 100 ~ 200 hPa) and extending into the stratosphere. Errors embedded in the multiple regression analysis, uncertainties associated with the reanalysis data, and the inaccuracies of the climate model can all affect the accuracies of the derived temperature variance. But the consistency among the tropospheric temperature variance from both reanalysis and climate model results gives us confidence to establish a solid standard error estimation baseline for temperature variance that is key to set the calibration requirement of CLARREO.

Fig. 5 also demonstrates that although ENSO and QBO make trivial contribution to the temperature variation in the stratosphere, their contribution below 100 hPa can be as large as 0.1 K. It should be noted that ENSO plays a much more dominant role than QBO in the troposphere as illustrated in Fig. 3. The σ_{var} value shown on the left panel of Fig. 5 is the standard deviation of the temperature residual after we subtract the linear trends and prescribed forcing effects from the time series data. The proper estimation of natural temperature variation also requires the autoregressive analysis to estimate the autocorrelation time, τ_{var}. Leroy et al. (2008a) presented a theoretical way to define an accurate way to calculate autocorrelation time, which requires the calculation of autocorrelation coefficients at all lags. A method by Weatherhead et al. (1998) have been widely used for the climate trend detection. Phojanamongkolkij et al. (2014) compared the two methods and concluded that the choice of the method depends on the auto correlation characteristics of the data. For simplicity, we follow the method used by Weatherhead et al. (1998) and treat the residual as a first-order autoregressive, AR(1), process. Different autocorrelation time values are plotted in the right panel of Fig. 5.

We use Eq. (3) to establish different CLARREO calibration requirements defined by σ_{var} and τ_{var} in Fig. 5. Fig. 6 shows the calculated σ_{cal}, given a trend accuracy uncertainty factor, U_a, of 1.2 and an instrument defined autocorrelation time, τ_{cal}, of 5 years. The value of U_a and τ_{cal} are chosen to be consistent with those used by Leroy et al. (2008a) and Wielicki et al. (2013). The most stringent calibration requirement comes from the observation requirement for low tropospheric temperature. Depending on whether we include the internal climate forcing (QBO and ENSO) as natural variability or not, the σ_{cal} ranges from 0.033 to 0.055 K (*k*=2, 95% confidence). It means that a CLARREO-like satellite system needs to achieve an observation accuracy of 0.033~0.055 K (*k*=2) for low tropospheric temperature to ensure the desired climate trend detection ability. The observation requirement for surface skin temperature trend detection is approximately 0.045 K (*k*=2) when QBO and ENSO contributions are excluded from the natural variability.

b. Water vapor

Similar to the analysis applied to temperature, we seek to decompose the water vapor in an observational time series with a multiple linear regression form, and investigate the attribution of the known climate forcing factors to the global water vapor variations. The naturally occurring water vapor variations can thus be given by subtracting the linear trend and associated climate forcing contributions from the globally distributed water vapor anomaly data,

$$\varepsilon = H(t) - a_0 t - a_1 E(t + \tau_1) \quad (7)$$

Our studies show that the dominant climate forcing factor that affects the water vapor variations in the troposphere region is the ENSO. Including volcanic contribution in Equation 7 produces insignificant difference. Li and Sharma (2013) concluded that although CMIP3 data show strong negative correlation between volcanic aerosol optical depth and water vapor, the reanalysis data only show weak correlation on a global scale, which is consistent with our finding. Fig. 7 and Fig. 8 demonstrate global average water vapor variation from MERRA and ECMWF ERA Interim. The poor agreement of long-term water vapor trend between the reanalysis outputs is well known, but reasonable agreement for short- term fluctuations can be expected (Dessler et al. 2010). The ENSO signals from two reanalysis models agree well since they correlate more strongly with short-term fluctuations than the long-term trend. The standard deviation plots demonstrated in Fig. 9 also show much better agreement between water vapor variations than the comparison between trends from the two reanalysis models. We apply a similar analysis as has been applied to the temperature anomalies in Section 2.1 to establish the observation requirements for the global water vapor trend study. The requirements are plotted in Fig. 11. Although there is a large discrepancy between the trend derived from ECMWF water vapor anomaly and that from MERRA, the ENSO signals extracted from both water vapor data sets are similar in scale. The magnitudes of the long-term water vapor natural variations obtained by subtracting the linear trend and the ENSO signals are in reasonable agreement.

3. IR Instrument Calibration Requirement Trade Study

The CLARREO IR instrument is designed to have sufficient spectral resolution, spectral coverage, and global spatial sampling so that the space-time averaged spectra can be used to "fingerprint" climate change signals. The radiometric calibration requirement for the CLARREO IR instrument is based on the consideration that the errors in the attributed climate signals introduced by the radiometric calibration inaccuracy should be less than the natural variability measurements requirements. The natural variability measurement requirements, predominantly driven by the requirements for temperature and the water vapor observations, are established in Section 2.1 and 2.2. We first derive the inverse relationship to quantify the attribution of the spectral radiance change to temperature and moisture, and then carry out a simulation study by using synthetic spectral errors that resemble realistic CLARREO instrument characteristics. A practical calibration requirement can thus be established by considering possible calibration errors due to low detector sensitivity and low optical transmittance near band edges and by checking the corresponding error introduced in temperature and moisture, using the natural variability measurement requirements as the reference.

The spectral dependent relationship between the outgoing IR radiation change and the temperature and water vapor fingerprints can be characterized as

$$\Delta \boldsymbol{R} = \boldsymbol{S}\boldsymbol{A} + \boldsymbol{r} \tag{8}$$

where ΔR represents the IR spectral fingerprints, S is the spectral signature (fingerprint) matrix, A represents the climate forcing factors, and r is the error vector that accounts for errors such as the radiation fluctuation caused by natural variability and the nonlinearity residual due to ignoring higher order contributions. For climate Observation Simulation Study Experiments (OSSEs) using different climate models, signal shape uncertainty is also included in $\boldsymbol{r}$ (Leroy et al. 2008b, Huang et al. 2010). Optimal detection techniques can be used to determine the amplitude of multiple climate signals with a prescribed signature matrix, S. The least square solution (Hasselmann, 1997) is given as

$$\boldsymbol{A} = (\boldsymbol{S}^T \boldsymbol{\Sigma}^{-1} \boldsymbol{S})^{-1} \boldsymbol{S}^T \boldsymbol{\Sigma}^{-1} \Delta \boldsymbol{R} \tag{9}$$

where Σ is the covariance of the residual r.

In this study, we take into account of the instrument calibration error in the inversion process explicitly. Our goal is to find out how much calibration error we can tolerate in order to detect a climate variable change to a required accuracy. The spectral calibration error, ΔR_{cal}, will introduce errors in the geophysical variables such as atmospheric temperature and moisture profiles

$$\Delta X = (\boldsymbol{S}^T \boldsymbol{\Sigma}^{-1} \boldsymbol{S})^{-1} \boldsymbol{S}^T \boldsymbol{\Sigma}^{-1} \Delta \boldsymbol{R}_{cal} \tag{10}$$

To have a direct illustration of the effect that spectral calibration errors imposed on the temperature and water vapor retrieval, spectral signatures of various climate-forcing factors can be decomposed into the linear combination of the radiance change due to the change of geophysical parameters associated with each corresponding climate-forcing factor:

$$\boldsymbol{SA} = \overline{\frac{dR}{dX} \boldsymbol{\Delta X}}. \tag{11}$$

Eq. (8) can thus be rewritten as

$$\overline{\boldsymbol{\Delta R}} = \overline{\boldsymbol{K \Delta X} + \boldsymbol{r_0'}} \tag{12}$$

where $\overline{\Delta R}$ is the space-time averaged radiance change, and K is the Jacobian (dR/dX) for instantaneous observation and defines the spectral shape and magnitude of the response of radiance to the change of atmospheric parameters. ΔX represents the change of atmospheric parameters at a certain geographical location after a certain observation time interval. Residual term r_0' is the nonlinear residual $[R(X + \Delta X) - R(X)] - K\Delta X$. Eq. (12) can be further expanded as:

$$\overline{\boldsymbol{\Delta R}} = \overline{\boldsymbol{K}}\overline{\boldsymbol{\Delta X}} + \overline{\boldsymbol{K}(\boldsymbol{\Delta X} - \overline{\boldsymbol{\Delta X}})} + \overline{\boldsymbol{r_0'}}. \tag{13}$$

The residual in Eq. (13) includes two parts: the space-time averaged radiance signal uncertainty due to the natural variability of atmospheric parameters and the space-time averaged nonlinearity errors. The optimal detection method can be used to give the solution:

$$\overline{\boldsymbol{\Delta X}} = (\overline{\boldsymbol{K}}^T \Sigma_s^{-1} \overline{\boldsymbol{K}})^{-1} \overline{\boldsymbol{K}}^T \boldsymbol{\Sigma}_s^{-1} \overline{\boldsymbol{\Delta R}} \tag{14}$$

where Σ_s is the covariance matrix that accounts for both post fit residuals in Eq. (13). Hence, the effect of calibration error (ΔR_{cal}) on the retrieved atmospheric parameters can be established as:

$$\Delta \boldsymbol{X}_{cal} = (\overline{\boldsymbol{K}}^T \boldsymbol{\Sigma}_s^{-1} \overline{\boldsymbol{K}})^{-1} \overline{\boldsymbol{K}}^T \boldsymbol{\Sigma}_s^{-1} \Delta \boldsymbol{R}_{cal}. \quad (15)$$

How ΔX_{cal} is affected by ΔR_{cal} can be partially illustrated by the spectral characteristics of the Jacobian, K. Fig. 11, Fig. 12, and Fig. 13 are sample plots of temperature, water vapor, and skin temperature Jacobians, respectively. We can see from Fig. 11 that spectral change in the narrow CO_2 absorption band (600 cm^{-1} ~ 800 cm^{-1}) can be attributed to the change in the vertical atmospheric temperature. Fig. 11 and Fig. 12 together show that observation errors of temperature and water profiles in the lower troposphere (about 200 *hPa* ~ 900 *hPa*) can be ascribed to radiance errors in the 200 cm^{-1} ~ 600 cm^{-1} and 1210 cm^{-1} ~ 2000 cm^{-1} wavenumber regions. The hyper-spectral feature of CLARREO allows the vertical profiling of atmospheric properties with high vertical resolution. We also expect that a CLARREO-like instrument can, under a wide range of cloudy sky conditions, provide atmospheric information from below clouds as long as the cloud optical depth is not too high. Fig. 14 plots the effective emissivity of water and ice clouds as a function of cloud optical depth. Even with cloud optical depth as high as 4, the effective cloud emissivity is less than 0.9 in most spectral regions (non-opaque). This conclusion is further supported by the non-zero values of the temperature, water vapor, and surface skin temperature Jacobians below clouds as shown in Fig. 11, Fig. 12, and Fig. 13. It should be noted that the cloud optical depth values are in reference to a visible wavelength at 550 nm. The infrared cloud optical depths can be estimated from the visible cloud optical depth according to the formula:

$$\tau(\nu) = \frac{\overline{Q_e(\nu)}}{Q_e(vis)}\tau(vis) \quad (16)$$

where τ is the optical thickness and Q_e is the cloud extinction coefficient, ν represents the infrared channel frequency, and vis represents the visible wavelength (550 nm). The infrared cloud optical depths are usually smaller than those at 550 nm because $Q_e(vis)$ is usually 2 and Q_e in the IR spectral region is usually smaller than 2. The Jacobians are shown as the change of top-of-atmosphere (TOA) brightness temperature (BT) to the change of the geophysical parameters. The upper left panels of Fig. 11, Fig. 12, and Fig. 13 illustrate a case with a cloud visible optical depth as thick as 3.95. The spectral signature of water vapor absorption from below the clouds is still clear (upper left panel of Fig. 12), and the contribution of surface emission to TOA radiance is non-negligible (upper left panel of Fig. 13), indicating non-opaqueness of the cloud.

The effect of spectrally dependent radiometric calibration errors of the CLARREO IR instrument on the fingerprints of the space-time averaged variations of temperature and water vapor vertical profiles, being mathematically expressed in Eq. 15, are estimated via simulation studies. We used a global atmospheric profile database (Borbas et al. 2005), which consists of 15704 globally selected temperature, water vapor, and ozone profiles at 101 vertical pressure levels. We chose this database because it was carefully selected from global radiosondes, ECMWF forecast profiles, and various other data sources (Susanne et al. 2007, Martins et al. 2017). Both temperature and water vapor profiles have large dynamic ranges and representative global coverage (Martins et al. 2017). There is no cloud information in the database, so we matched these atmospheric profiles with various cloud conditions, including clear sky, thin cloud, and opaque cloud cases. The phase of the cloud is determined according to the temperatures at the cloud altitude. The cloud optical depth at 550 nm and cloud particle sizes are randomly assigned. The ranges of effective radius for water and ice clouds are 2.5-15 micrometers and 5-35 micrometers, respectively. We use a fast principal component based radiative transfer model (PCRTM) to simulate TOA radiance and generate the Jacobians associated with the temperature, water vapor, surface properties and cloud parameters (Liu et al., 2006, 2009, 2016, Yang et al. 2016). The advantages of the PCRTM model include fast computational speed and high accuracy. It takes about 0.06 of a second to compute one CLARREO radiance spectrum using an Intel 1.6 GHz CPU. The Root-mean-squares errors of the PCRTM model relative to a line-by-line radiative transfer model (Clough et al. 1992) are less than 0.03 K. The fast speed of the PCRTM is achieved by compressing the CLARREO spectra into the Principal Component (PC) domain and by removing redundant radiative transfer calculations at numerous monochromatic frequencies (Liu et al 2006). For the CLARREO IR instrument with 0.5 cm^{-1} spectral resolution, only a few hundred monochromatic radiative transfer calculations are needed to accurately represent the whole spectrum. PCRTM has been used to retrieve atmospheric and cloud properties from hyperspectral IR measurements (Liu et al., 2009) and in an atmospheric fingerprinting study (Kato et al., 2011). PCRTM provides analytical solutions of the Jacobians as direct outputs and is a well-suited tool for the calibration study presented here.

Numerically, the Jacobian, *K*, is a linear approximation for radiative transfer equations. $\bar{K}^T \Sigma_s^{-1} \bar{K}$ is usually ill-conditioned and regularization is needed to solve for ΔX in Eq. (15). We have applied two constraints in our spectral fingerprinting process. One is to reduce correlations between matrix elements by projecting temperature and moisture vertical profiles onto Principal Component (PC) space as describe by Liu et al (2009). The other one is to add the Tikhonov regularization to the cost function. By converting the profiles into PC-space using selected leading principal components, we can improve the conditional number of the $\bar{K}^T\Sigma_s^{-1}\bar{K}$ matrix. In this study, the vertical temperature and water vapor profiles have 101 pressure levels when calculating the Jacobian matrix, K. After PC-compressing, we only need to retain 20 temperature PC scores and 15 water vapor PC scores. The Tikhonov regularization method, if applied here to find the solution to Eq. (15), amounts to finding the solution of ΔX which gives a least-square fit to ΔR, but penalizes solutions by minimizing the cost function

$$(\bar{K}^T\Delta X - \Delta R)^T\Sigma_s^{-1}(\bar{K}^T\Delta X - \Delta R) + \|\Gamma\Delta\boldsymbol{X}\|^2 \quad (17)$$

The solution to Eq. (15) can be rewritten as

$$\overline{\Delta\boldsymbol{X}} = (\bar{K}^T\Sigma_s^{-1}\bar{K} + \Gamma^T\Gamma)^{-1}\bar{K}^T\Sigma_s^{-1}\overline{\Delta\boldsymbol{R}} \quad (18)$$

with the calibration error being introduced as

$$\Delta\boldsymbol{X}_{cal} = (\bar{K}^T\Sigma_s^{-1}\bar{K} + \Gamma^T\Gamma)^{-1}\bar{K}^T\Sigma_s^{-1}\Delta\boldsymbol{R}_{cal}. \quad (19)$$

The Tikhonov matrix, Γ, is introduced here to improve the matrix condition of $\bar{K}^T\Sigma_s^{-1}\bar{K}$ and in many cases is chosen as a multiple of the identity matrix, I, such that $\Gamma = \lambda I$. The damping factor, λ, is chosen in the way that the subspaces of the kernel matrix $\bar{K}^T\Sigma_s^{-1}\bar{K}$ with smallest singular values can be dampened so that the inversion operation will not amplify the contribution of trivial features. We adopt a regularization scheme that employs different damping factors for temperature and water vapor of the kernel matrix $\bar{K}^T\Sigma_s^{-1}\bar{K}$. The scheme is based on our experience in temperature and water vapor retrievals using hyperspectral data such as IASI (Liu et al 2009). Since the atmospheric temperature and water profiles have different units and they are compressed into Principal Component (PC) domain, the state vector (X) elements have large difference in values. To reduce the contributions from PCs with small scores, we take the diagonal elements of the regularization matrix, which correspond to temperature and water vapor elements, to be the mean values of the corresponding diagonal elements of the $\overline{\mathrm{K}}^{\mathrm{T}}\Sigma_{\mathrm{s}}^{-1}\overline{\mathrm{K}}$ matrix. We always check our posterior fiting error in the spectral domain to ensure that they are smaller than the calibration errors.

With the inversion relationship defined by Eq. (15) being established, we carried out a series of spectral fingerprinting trade studies by assuming different instrument calibration errors. Fig. 15 plots a 0.04 K (k=2) radiometric calibration error and the corresponding fingerprinting errors. The blue solid line on the top panel shows the 0.04 K spectrally independent calibration error. The corresponding errors (k=2) introduced in temperature and water vapor vertical profiles are shown as solid blue curves on the bottom left and right panels. As a reference, the calibration requirements for temperature and water vapor that have been derived from the MERRA, ECMWF, and GFDL CM3 data sets are plotted as dashed lines in the lower panels. The 0.04 K (k=2) calibration error is marginally tolerable because the corresponding fingerprint error in near surface temperature is approaching the calibration requirement defined by MERRA and ECMWF data.

In this study, we assume that the CLARREO IR FTS (Mlynczak, 2010) will use a pyroelectric detector for its far-infrared band (Band 1: 200 cm^{-1} ~ 645 cm^{-1}) and photoconductive or photovoltaic mercury cadmium telluride (MCT) detectors for its two infrared bands (Band 2: 645 cm^{-1} ~ 1210 cm^{-1}, Band 3: 1210 cm^{-1} ~ 2000 cm^{-1}). Usually, calibration errors tend to be larger at the spectral band edges due to larger instrument response uncertainties. We expect larger errors near 200 cm^{-1} due to the low transmittance of the beam splitter and larger errors near 645 cm^{-1}, 1210 cm^{-1}, and 2000 cm^{-1} due to the band edge effect of the MCT detector and optical filters used for each band. Considering that the pyroelectric detector has sensitivity extending to the mid-IR, we can assume that there is no band edge effect to the left of 645 cm^{-1}. The red curve on the middle panel of Fig. 15 represents a more realistic, spectrally dependent calibration error curve of the CLARREO IR instrument. The corresponding spectral fingerprinting error for temperature and water vapor vertical profiles are shown as solid red curves on the bottom left and right panels of Fig. 15.

By comparing the effects of calibration errors shown as blue and red lines in the lower panels of Fig. 15, we can see that the large band edge errors in the P-branch of the CO_2 spectral region (near 650 cm^{-1}) can be tolerated due to the redundant spectral information carried by the R-branch CO_2 spectral region. The spectral regions near 1210 cm^{-1} and 2000 cm^{-1} contain spectral channels mainly sensitive to surface and cloud properties. Our studies show that as long as we include the error estimation for these spectral regions in the error covariance matrix, Σ_S, the surface skin temperature and cloud property retrievals are not impacted by them, again due to the redundant information from other surface and cloud-sensitive channels. The spectral-dependent red curve shown in the middle panel of Fig. 14 is a stringent calibration accuracy requirement that can ensure that CLARREO's observation accuracy for climate trend detection falls within 20% of the accuracy of a perfect system. The observation accuracy for low tropospheric temperature will be better than 0.04 K (k=2) and that for the stratospheric temperature should be 0.08 K (k=2). The water vapor observation error near surface will be smaller than 0.03 g/kg (k=2).

The value of a CLARREO-like observation system with a 0.04 K (k=2) calibration accuracy in climate trend detection can be illustrated by plotting the dependence of low tropospheric temperature (at 975 hPa) trend detection uncertainty on instrument calibration accuracy (shown in Fig. 16). The curves are calculated using a 0.25 K (k=2) temperature variance and a 3 month autocorrelation time which are obtained from the ECMWF data (plotted as a dashed green curve in Fig. 5). Using values obtained from MERRA data will give similar results. We can see from Fig. 16 that a perfect observation system needs about 12.3 years in order to reach a trend detection uncertainty of 0.1 K/decade, while a system with a 0.04 K calibration accuracy requires 13.7 years, lagging 1.4 years behind. Changing the calibration accuracy requirement to 0.06 K (k=2) means 15.1 years are needed to reach the 0.1 K/decade trend detection uncertainty, further delaying the trend detection time by another 1.4 years.

Graphs like those in Fig. 16 are useful in studying the synergistic usage of the CLARREO IR instrument and operational sounders. The current hyperspectral IR sounders have provided valuable data for improving Numerical Weather Prediction (NWP) forecasts for many years and the data records will continue for many decades. However, since these sounders were designed for weather applications, the radiometric calibration specifications of these instruments are less accurate as compared to the CLARREO IR instrument. As referenced in Wielicki et al (2013), the absolute accuracy of the operational sounders such as CrIS, AIRS, and IASI ranges from 0.2 to 0.4 K (k=2). Wang et al. (2015) have compared the radiometric consistency of the CrIS, the IASI-A and IASI-B on Meteorological Operational satellites, and the AIRS using one year (2013) of simultaneous nadir overpass data. They concluded that the radiometric consistency between CrIS and IASI is on the order of 0.1 to 0.2 K (68% confidence level, k=1) for longwave IR (LWIR) band and mid-wave IR (MWIR) band. For CrIS and AIRS, the LWIR and MWLR differences are around 0.1 K (k=1) for most of the spectrally averaged regions they have studied. For some spectral regions in LWIR and MWIR, the differences are in the range of 0.15 to 0.21 K (k=1). The radiometric differences between these four instruments in the shortwave IR band are larger as compared to the LWIR and MWIR bands. Using Figure 16, we can compare detection times needed to accurately determine near surface atmospheric temperature using various satellite instruments. For the purpose of quantitative comparison, we assume that the absolute calibration accuracy of the CrIS, AIRS, and IASI is about 0.24 K (*k*=2). It will take 30 years of operation time to achieve the temperature detection uncertainty of 0.1 K/decade. This means that a CLARREO-like instrument with a 0.04 K (*k*=2) calibration accuracy can save more than 16 years as compared with existing hyperspectral IR systems. Furthermore, if a CLARREO IR Pathfinder instrument is mounted on International Space Station with the CLARREO RS Pathfinder instrument, or if a CLARREO IR instrument is mounted on a free-flyer, we will be able to perform on-orbit inter-satellite calibration and reduce the calibration uncertainty of the sounder instruments. We can then take advantages of the sounders' long time records and more diverse temporal and spatial coverages to further improve the accuracy of the global temperature climate trend detection.

It should be noted that the CLARREO IR instrument not only has SI-traceable blackbody temperature measurements, it also has an independent onboard verification system to check absolute calibrations at various scene temperatures. The highly accurate hyperspectral radiance spectra observed by the CLARREO IR instrument can be used as absolute references for inter-satellite calibration and can be used to identify potential error sources such as the blackbody temperature measurement and non-linearity correction. Since the operational sounders provide swath widths larger than 2000 km, we will have improved diurnal sampling and spatial sampling for climate trend detection by leveraging the CLARREO inter-calibrated sounder data, The combined data will provide better characterization of climate changes in different climate zones or regions, which in turn will provide a detection for global temperature and water vapor changes.

Our study demonstrates that atmospheric temperature trend observations between the middle troposphere and the stratosphere region are less sensitive to instrument calibration error than that between the surface and low troposphere region since the temperature natural variability are larger in the upper atmosphere. Fig. 17 shows the impact of instrument calibration errors on the delay of climate trend detection in stratospheric temperature at 70 hPa. If we assume a 0.48 K (k=2) natural variability and an autocorrelation time of 5.6 months that come from the GFDL CM3 simulation, a system with a 0.06 K (k=2) calibration accuracy will save more than 10 years of operational time to achieve a 0.1 K/decade (k=2) trend uncertainty as compared with the current IR instruments in orbit, and will only lag behind a perfect observation system by one year.

The impact of instrument calibration accuracy on the surface water vapor trend observation is illustrated in Fig. 18. A significant global-scale increase in surface water vapor has been identified (Dai, 2006, Willett et al., 2007), and the reported global surface water vapor anomalies are in a similar scale to the water vapor anomaly derived from MERRA data (shown in Fig. 8). By taking the linear trend difference (about 0.1 g/kg/decade) between the MERRA result and the ECMWF result (red lines in Fig. 8) as a rough estimation for the surface water vapor trend uncertainty, a system with a 0.06 K

(k=2) calibration accuracy has the potential to reduce the detection time by more than 6 years relative to the current IR instruments in orbit.

4. Conclusions

We have studied the spectrally dependent radiometric calibration requirement of the CLARREO IR instrument based on the climate trend detection uncertainty requirement. The validity of the presented calibration requirement depends on the accuracy of the reanalysis and the climate model data from which the magnitude of naturally occurring variations are calculated. Our analysis shows a good agreement between the temperature variance derived from ERA-Interim data and that from MERRA data. Also demonstrated is the consistency between the reanalysis results and the GFDL CM3 climate model results in the troposphere region which validates the use of multiple-regression to obtain reliable natural variability free of major forcing factors. Although the uncertainty of temperature variance in the stratosphere is large -- the discrepancy between reanalysis variability and GFDL CM3 variability in the stratosphere can be bigger than 100%-- only a narrow spectral region's calibration requirement is associated with the stratospheric temperature observation requirement. The differences in the prescriptions of water vapor variance, especially those between reanalyses and the GCM, introduce uncertainty in the calibration requirement for monitoring tropospheric water vapor in the infrared spectra; however, our simulation study demonstrates that the radiometric calibration requirement imposed by the atmospheric temperature trend observation needs will be more stringent than that derived from the most conservative water vapor natural variability value. It is the observation requirement for the temperature of the troposphere and surface that determines the spectral calibration baseline in the IR measurement band.

The 0.04 K (k=2, 95% confidence level) calibration baseline demonstrated in Fig. 15(b) is established based on a given uncertainty factor (U_a = 1.2). It can be viewed as a conservative and stringent solution. The natural variability values used here are obtained after subtracting the contributions of volcanic eruptions, solar cycle, ENSO, and QBO from the temperature and water vapor anomalies. Our study is based on the assumption that the climate fingerprints of ENSO and QBO can be effectively and accurately separated from the climate anomalies. If QBO and ENSO (especially ENSO, which is a key climate forcing factor contributing to the low tropospheric temperature variation) are included as part of the natural variability, the magnitude of the temperature variance will be larger, as can be seen from the difference between the dashed curves and the solid curves in Fig. 5. The corresponding temperature calibration requirement will be relaxed to 0.055 K (k=2) in the troposphere region. Whether to include ENSO-caused water vapor fluctuations as a part of the naturally occurring process or not has negligent impact on calibration requirements for water vapor observations (shown in Fig. 9 and Fig. 10). Following the same inversion process described in Section 3, the relaxed temperature calibration requirement will transfer into a less stringent spectral calibration requirement of 0.06 K (k=2).

The calibration requirement study here is based on the temperature and water vapor data with statistics obtained from NWP reanalysis data and climate model simulation results. The demonstrated spectral calibration baseline is established as a ‘safe’ estimation that can be adjusted based on the finalization of the trend observation uncertainty requirement and the potential improvement in the accuracy of natural variability values in the future. The calibration trade study methodology presented in Section 3 can be used for any future calibration requirement study based on the observation requirement for other key climate change parameters such as clouds and CO_2. The current study mainly focused on the spectral fingerprinting and we used global mean anomalies to derive atmospheric temperature and water vapor natural variabilities. It should be noted that a lot of information is available in the spatial patterns of the climate signals. In the future, we will perform Observing System Simulation Experiments (OSSEs) using either ERA-interim or MERRA to detect climate trends in different climate regions and to study the longwave radiative feedbacks using CLARREO IR spectra.

*Acknowledgments***.**

This research was supported by the NASA CLARREO project. The NASA SMD High-End Computing (HEC) resources were used to support the PCRTM radiative transfer model development.

REFERENCES

Angell, J. K., 2000: Tropospheric temperature variations adjusted for El Niño, 1958- 1998. *J. Geophys. Res*., **105**, 11841–11849, doi:10.1029/2000JD900044.

Borbas, E. E.; Seemann, S. W.; Huang, H. L.; Li, J.; Menzel, W. P., 2005: Global profile training database for satellite regression retrievals with estimates of skin temperature and emissivity. In International TOVS Study Conference-XIV Proceedings.

Chiodo, G., D. R. Marsh, R. Garcia-Herrera, N. Calvo, and J. A. Garcia, 2014: On the detection of the solar signal in the tropical stratosphere. *Atmospheric Chemistry and Physics*, **14**, 5251-5269, doi: 10.5194/acp-14-5251-2014.

Clough, S.A., M.J. Iacono, and J.-L. Moncet, 1992: Line-by-line calculation of atmospheric fluxes and cooling rates:Application to water vapor.*J. Geophys. Res.*, **97**, 15761-15785.

Crooks, S. A. and L. J. Gray, 2005: Characterization of the 11-Year Solar Signal Using a Multiple Regression Analysis of the ERA-40 Dataset. *J. Climate*, **18**, 996–1015, doi:10.1175/JCLI-3308.1

Dai, A. 2006: Recent Climatology, Variability, and Trends in Global Surface Humidity. *J. Climate,* **19**, 3589–3606, doi: 10.1175/JCLI3816.1.

Dee, D. P., Uppala, S. M., Simmons, A. J., Berrisford, P., Poli, P., Kobayashi, S., Andrae, U., Balmaseda, M. A., Balsamo, G., Bauer, P., Bechtold, P., Beljaars, A. C. M., van de Berg, L., Bidlot, J., Bormann, N., Delsol, C., Dragani, R., Fuentes, M., Geer, A. J., Haimberger, L., Healy, S. B., Hersbach, H., Hólm, E. V., Isaksen, L., Kållberg, P., Köhler, M., Matricardi, M., McNally, A. P., Monge-Sanz, B. M., Morcrette, J.-J., Park, B.-K., Peubey, C., de Rosnay, P., Tavolato, C., Thépaut, J.-N. and Vitart, F. (2011), The ERA-Interim reanalysis: configuration and performance of the data assimilation system. *Q. J. R. Meteorol. Soc.*, **137**, 553–597, doi:10.1002/qj.828

Dessler, A. E., *and* S. M. Davis, 2010: Trends in tropospheric humidity from reanalysis systems. *J. Geophys. Res.*, **115**, 19127, *doi:*10.1029/2010JD014192.

Donner, Leo J., et al. 2011: The dynamical core, physical parameterizations, and basic simulation characteristics of the atmospheric component AM3 of the GFDL global coupled model CM3, *Journal of Climate*, **24**, 3484-3519, doi:10.1175/ 2011JCLI3955.1.

Foster, G., and S. Rahmstorf, 2011: Global temperature evolution 1979–2010. *Environ. Res. Lett.*, **6**, 044022, doi:10.1088/1748-9326/6/4/044022.

Hasselmann, K., 1997: Multi-pattern fingerprint method for detection and attribution of climate change. *Clim. Dyn.*, **13**, 601–611, doi:10.1007/s003820050185.

Huang, Y., S. Leroy, P. J. Gero, J. Dykema, and J. Anderson, 2010: Separation of longwave climate feedbacks from spectral observations. *J. Geophys. Res.*, **115**, D07104, doi:10.1029/2009JD012766.

Kato S., B. A. Wielicki, F. G. Rose, X. Liu, P. C. Taylor, D. P. Kratz, M. G. Mlynczak, D. F. Young, N. Phojanamongkolkij, S. Sun-Mack, W. F. Miller, and Y. Chen, 2011: Detection of Atmospheric Changes in Spatially and Temporally Averaged Infrared Spectra Observed from Space. *J. Climate*, **24**, 6392–6407, doi:10.1175/JCLI-D-10-05005.1

Lean, J. L., and D. H. Rind, 2008: How natural and anthropogenic influences alter global and regional surface temperatures: 1889 to 2006. *Geophys. Res. Lett.*, **35**, *L18701, doi:*10.1029/2008GL034864.

Leroy S. S., J. G. Anderson, and G. Ohring, 2008a: Climate Signal Detection Times and Constraints on Climate Benchmark Accuracy Requirements. *J. Climate*, **21**, 841–846. doi:10.1175/2007JCLI1946.1.

Leroy S. S., J. G. Anderson, J. Dykema, and R. Goody, 2008b: Testing Climate Models Using Thermal Infrared Spectra. *J. Climate*, **21**, 1863–1875, doi:10.1175/2007 JCLI2061.1

Li, J., and A. Sharma, 2013: Evaluation of volcanic aerosol impacts on atmospheric water vapor using CMIP3 and CMIP5 simulations, J. Geophys. Res. Atmos., 118, 4448–4457, doi:10.1002/jgrd.50420.

Liu X., W. L. Smith, D. K. Zhou, and A. M. Larar, 2006: Principal component-based radiative transfer model for hyperspectral sensors: theoretical concept. *Appl. Opt*. **45**, 201-209, doi:10.1364/AO.45.000201.

Liu, X., D. K. Zhou, A. M. Larar, W. L. Smith, P. Schluessel, S. M. Newman, J. P. Taylor, and W. Wu, 2009: Retrieval of atmospheric profiles and cloud properties from IASI spectra using super-channels. *Atmos. Chem. Phys.*, **9**, 9129–9142, doi:10.5194/acp-9-9121-2009.

Liu, X., D. K. Zhou, Allen Larar, W. L. Smith, and S. A. Mango, 2007: Case Study a New Radiative Transfer Model and Retrieval Algorithm using EAQUATE Data, *Q. J. R. Meterol. Soc.*, **133**, 243-256, doi: 10.1002/qj.156.

Liu, X., Q. Yang, H. Li, Z. Jin, W. Wu, S. Kizer, D. K. Zhou, and P. Yang, 2016: Development of a fast and accurate PCRTM radiative transfer model in the solar spectral region, Appl. Opt. 55(29), 8236–8247.

Martins, J.P.A.; Trigo, I.F.; Bento, V.A.; da Camara, C. A, 2016: Physically Constrained Calibration Database for Land Surface Temperature Using Infrared Retrieval Algorithms. *Remote Sens.*, *8*, 808.

Mlynczak, M. G., 2010: Infrared Instrument Overview, CLARREO Science Meeting, Hampton, VA. [Available online at *http://clarreo.larc.nasa.gov/workshops/2010STM/Wednesday/IR_Final_Mlynczak.pptx*.

Philander, S. G. H., R. C. Pacanowski, N-C. Lau, and M. J. Nath, 1992: Simulation of ENSO with a Global Atmospheric GCM Coupled to a High-Resolution, Tropical Pacific Ocean GCM. *J. Climate,* **5**, 308–329, doi:10.1175/1520-0442(1992)005<0308:SOEWAG>2.0.CO;2.

Pajanamongkolkij, N., S. Kato, B. Wielicki, P. C. Taylor, and M. Mlynczak, 2014: A Comparison of Climate Signal Trend Detection Uncertainty Analysis Methods, J. Climate, 27, 3363-3376, doi:http://dx.doi.org/10.1175/JCLI-D-13-00400.1.

Powell A., and J. Xu, 2013: Evaluation of the temperature trend and climate forcing in the pre- and post periods of satellite data assimilation. *Satellite-based Applications on Climate Change*, J. Qu, A. Powell, M.V.K. Sivakumar, Eds., Springer, 49-65

Ramaswamy, V., *and Coauthors,* 2001*:* Stratospheric temperature trends: Observations and model simulations. *Rev. Geophys*., **39**, 71–122, *doi:*10.1029/1999RG000065.

Rienecker, M.M., M.J. Suarez, R. Gelaro, R. Todling, J. Bacmeister, E. Liu, M. G. Bosilovich, S. D. Schubert, L. Takacs, G.-K. Kim, S. Bloom, J. Chen, D. Collins, A. Conaty, A. da Silva, et al. (2011), MERRA: NASA's Modern-Era Retrospective Analysis for Research and Applications. *J. Climate*, **24**, 3624-3648, doi:10.1175/JCLI-D-11-00015.1

Santer, B. D., T. M. L. Wigley, C. Doutriaux, J. S. Boyle, J. E. Hansen, P. D. Jones, G. A. Meehl, E. Roeckner, S. Sengupta, *and* K. E. Taylor, 2001*:* Accounting for the effects of volcanoes and ENSO in comparisons of modeled and observed temperature trends. *J. Geophys. Res*., **106**, 28033–28059, doi:10.1029/2000JD000189.

Santer, B. D., and Coauthors, 2011: Separating signal and noise in atmospheric temperature changes: The importance of timescale. *J. Geophys. Res.*, **116**, D22105, doi:10.1029 /2011JD016263.

Sato, M., J. E. Hansen, M. P. McCormick, *and* J. B. Pollack, 1993*:* Stratospheric aerosol optical depths, 1850–1990*. J. Geophys. Res*., **98**, 22987–22994, doi:10.1029/ 93JD02553.

Seemann, S. W., Borbas, E. E., Knuteson, R. O., Stephenson, G. R., and Huang, H.-L., 2008: Development of a global infrared land surface emissivity database for application to clear-sky sounding retrievals from multi-spectral satellite radiance measurements, J. Appl. Meteorol. Clim., 47, 108–123.

Takahashi, M., 1999: Simulation of the quasi-biennial oscillation in a general circulation model, *Geophys. Res. Lett*., **23**, 661–664,. doi: 10.1029/1999GL900188

Taylor, K. E., R. J. Stouffer, and G. A. Meehl, 2009: A Summary of the CMIP5 Experiment Design. Accessed 18 December 2009. [Available online at http://cmip-pcmdi.llnl.gov/cmip5/docs/Taylor_CMIP5_design.pdf.*]*

Wang L., Y. Han, X. Jin, Y. Chen, D. A. Tremblay, 2015: Radiometric consistency assessment of hyperspectral infrared sounders, *Atmos. Meas. Tech., 8, 4831-4844.*

Weatherhead, E. C., and Coauthors, 1998: Factors affecting the detection of trends: Statistical considerations and applications to environmental data. *J. Geophys. Res.*, **103**, 17149–17161, doi:10.1029/98JD00995.

Wielicki, B. A., and Coauthors, 2013: Achieving Climate Change Absolute Accuracy in Orbit. *Bull. Amer. Meteor. Soc.*, **94**, 1519–1539, doi:10.1175/BAMS-D-12-00149.1.

Wigley, T. M. L., 2000: ENSO, volcanoes and record-breaking temperatures. *Geophysical Research Letters*, **27**, 4101-4104, doi:10.1029/2000GL012159.

Willett, K. M., N. P. Gillett, P. D. Jones, and P. W. Thorne, *Nature*, **449**, 710-712, doi:10.1038/nature06207

Wolter, K. and M. S. Timlin, 2011: El Niño/Southern Oscillation behavior since 1871 as diagnosed in an extended multivariate ENSO index (MEI.ext). *Int. J. Climatol*., **31**, 1074–1087, doi:10.1002/joc.2336.

Yang, Q., X. Liu, W. Wu, S. Kizer, and R. R. Baize, 2016: Fast and accurate hybrid stream PCRTM-SOLAR radiative transfer model for reflected solar spectrum simulation in the cloudy atmosphere, Optics Express 24, A1514-A1527. https://doi.org/10.1364/OE.24.0A1514

LIST OF TABLES

TABLE 1. Statistics of surface skin temperature variability (U_a=1.2, τ_{cal}=5 years)

Tskin anomaly	σ_{var} (K)	τ_{var} (month)	σ_{cal} (K)
ECMWF (free of external forcing)	0.27	4.4	0.045
MERRA (free of external forcing)	0.28	5.1	0.054
GFDL CM3 (pi-Control run)	0.31	8.6	0.078
ECMWF (free of all forcing)	0.24	3.1	0.041
MERRA (free of all forcing)	0.24	3.4	0.045

LIST OF FIGURES

Fig. 1. Flow Diagram describing the procedures used in Section 2 and Section 3.

Fig. 2. Global air temperature anomaly at 70 hPa derived using MERRA (left column) and ERA-Interim (right column) data. The subplots in the first row illustrate the temperature anomaly without accounting for ENSO, volcanic eruption, and solar cycle effects (blue curves), temperature anomaly after the subtraction of the volcanic eruption effect and the solar signals (dark green curves), and the derived linear trend (red lines) after the subtraction. Regression based estimations for ENSO (red curves), volcanic influence (black curves), solar signal (green curves), and QBO (cyan curves) are plotted in the second, the third, the fourth, and the fifth rows, respectively.

Fig. 3. Global air temperature anomaly at 975 hPa derived using MERRA (left column) and ERA-Interim (right column) data. See Figure 2 caption for more details.

Fig. 4. Similar to Figure 3 but for the global surface skin temperature anomaly derived using MERRA (left column) and ERA-Interim (right column) data. See Figure 3 caption for more details.

Fig. 5. Standard deviation of the temperature anomaly residual derived from MERRA, ECMWF reanalysis, and GFDL CM3 data. Left panel: Blue and green solid curves

– standard deviation derived for MERRA and ECMWF temperature anomaly free of volcanic and solar forcing; Red solid curve – variance of GFDL CM3 temperature; Blue and green dashed curves – standard deviation of MERRA and ECMWF reanalysis obtained after subtracting the linear trend and all four major climate forcing influences. Right Panel: Corresponding autocorrelation time, τ_{var}, calculated using the first-order autoregressive (AR1) model. The legend for the curves on the right panel is the same as those shown on the left panel.

Fig. 6. Calibration requirement associated with the temperature variance and the autocorrelation time shown in Figure 5, given a trend accuracy uncertainty factor, U_a, of 1.2 and an instrument defined autocorrelation time, τ_{cal}, of 5 years.

Fig. 7. Global water vapor anomaly at 800 hPa derived using MERRA (left column) and ERA-Interim (right column) data. The subplots in the top row illustrate the water vapor anomaly without accounting for ENSO effects (blue curves), water vapor anomaly after the subtraction of ENSO effects (dark green curves), and the derived linear trend (red lines) after the subtraction. Regression based estimations for ENSO (red curves) signals are plotted in the bottom row.

Fig. 8. Same as Figure 7 but for the global water vapor anomaly at 1000 hPa derived using MERRA (left column) and ERA-Interim (right column) data.

Fig. 9. Left panel: Standard deviation of the water vapor anomaly derived from the MERRA (blue curves) and the ECMWF reanalysis (green curves). Solid curves – standard deviation derived from the global average water vapor times series data; Dashed curves – standard deviation calculated after the subtraction of the ENSO signal. Red curve - standard deviation for GFDL water vapor. Right panel: corresponding lag 1 autocorrelation time.

Fig. 10. Calibration requirement associated with the water vapor variance and the autocorrelation time shown in Figure 9, given a trend accuracy uncertainty factor, U_a, of 1.2 and an instrument defined autocorrelation time, τ_{cal}, of 5 years.

Fig. 11. Temperature Jacobian (dBT/dT, BT - Brightness Temperature, T – air temperature) plots under different sky conditions. Upper left: Cloud located at 106.6 hPa with a visible optical depth of 3.95. Upper right: Cloud located at 205.5 hPa with a visible optical depth of 2.21. Lower left: Cloud located at 397.0 hPa with a visible optical depth of 1.36. Lower right: Clear sky.

Fig. 12. Water vapor Jacobian (dBT/dlog(h2o)) plots under different sky conditions. Upper left: Cloud located at 106.6 hPa with a visible optical depth of 3.95. Upper right: Cloud located at 205.5 hPa with a visible optical depth of 2.21. Lower left: Cloud located at 397.0 hPa with a visible optical depth of 1.36. Lower right: Clear sky.

Fig. 13. Same as Fig. 11 and 12 but showing sample Jacobian plots for surface skin temperature (dBT/dTskin).

Fig. 14. Water and ice cloud emissivity in the CLARREO IR measurement band as functions of cloud visible optical depth (at 500 nm wavelength), $\boldsymbol{\tau}$.

Fig. 15. The calibration errors and the corresponding errors introduced in temperature and water vapor observation. Upper panels: Spectral calibration error in brightness temperature (a. blue solid curve – 0.04 K (k=2) baseline error; b. red solid curve – potential calibration error based on a 0.04 K (k=2) baseline with detection band edge errors added); Lower panels: Corresponding calibration introduced temperature (c) and water vapor (d) fingerprinting errors (solid lines in matched colors). Calibration requirements for temperature and water vapor based on natural variability estimation results are plotted as dashed lines in lower panels as references: $\sigma_{cal\ ECMWF}$ –derived from ECMWF reanalysis data, $\sigma_{cal\ MERRA}$ – derived from MERRA data, $\sigma_{cal\ GFDL}$ – derived from GFDL CM3 data. These calibration requirements are also plotted in Figs. 6 and 10.

Fig. 16. Illustration of the dependence of the time to detect the low troposphere temperature trend on the observation systems' absolute calibration accuracy (95% confidence). The relationships calculated using the temperature natural variability values obtained when QBO and ENSO contributions are excluded from the natural variability: σ_{var} = 0.25 K, $\boldsymbol{\tau}_{\mathrm{var}}$ = 3.0 months (95% confidence

Fig. 17. Illustration of the dependence of the time to detect the stratospheric temperature (at 70 hPa with σ_{var} = 0.48 K, $\boldsymbol{\tau}_{\mathrm{var}}$ = 5.6 months (95% confidence)) cooling trend on the observation systems' calibration accuracy (95% confidence).

Fig. 18. Illustration of the dependence of the time to detect the specific surface humidity (at 1000 hPa with σ_{var} = 0.17 g/kg, $\boldsymbol{\tau}_{\mathrm{var}}$ = 9.6 months (95% confidence)) trend on the observation systems' calibration accuracy (95% confidence).

Section 2 Defining global temperature and water vapor trend detection

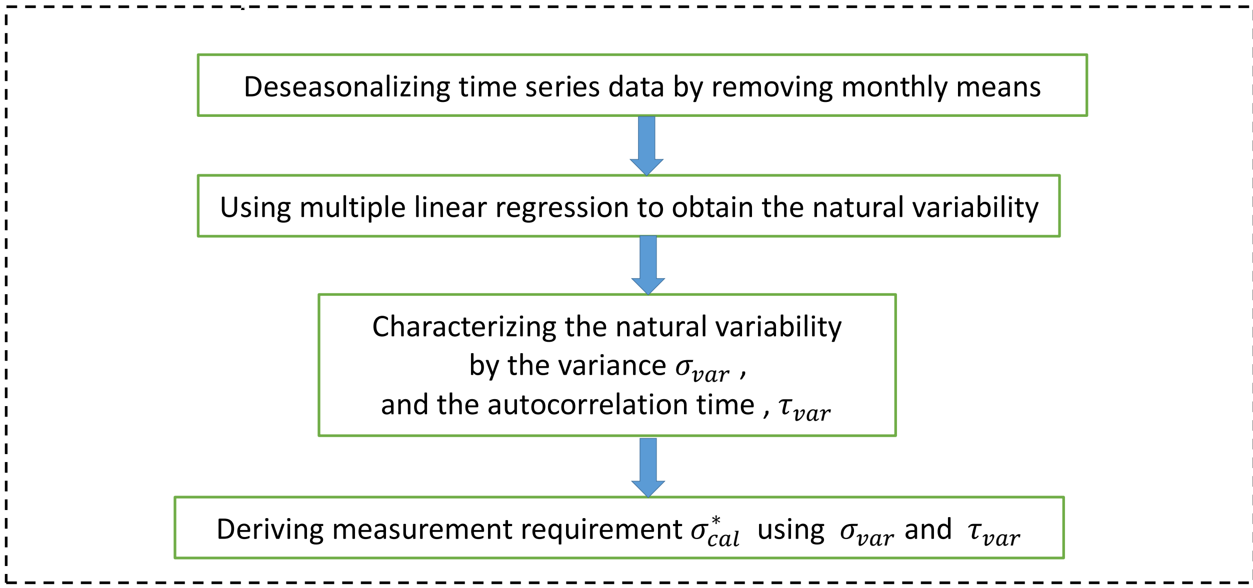

Section 3 Instrument Calibration Requirement Trade Study

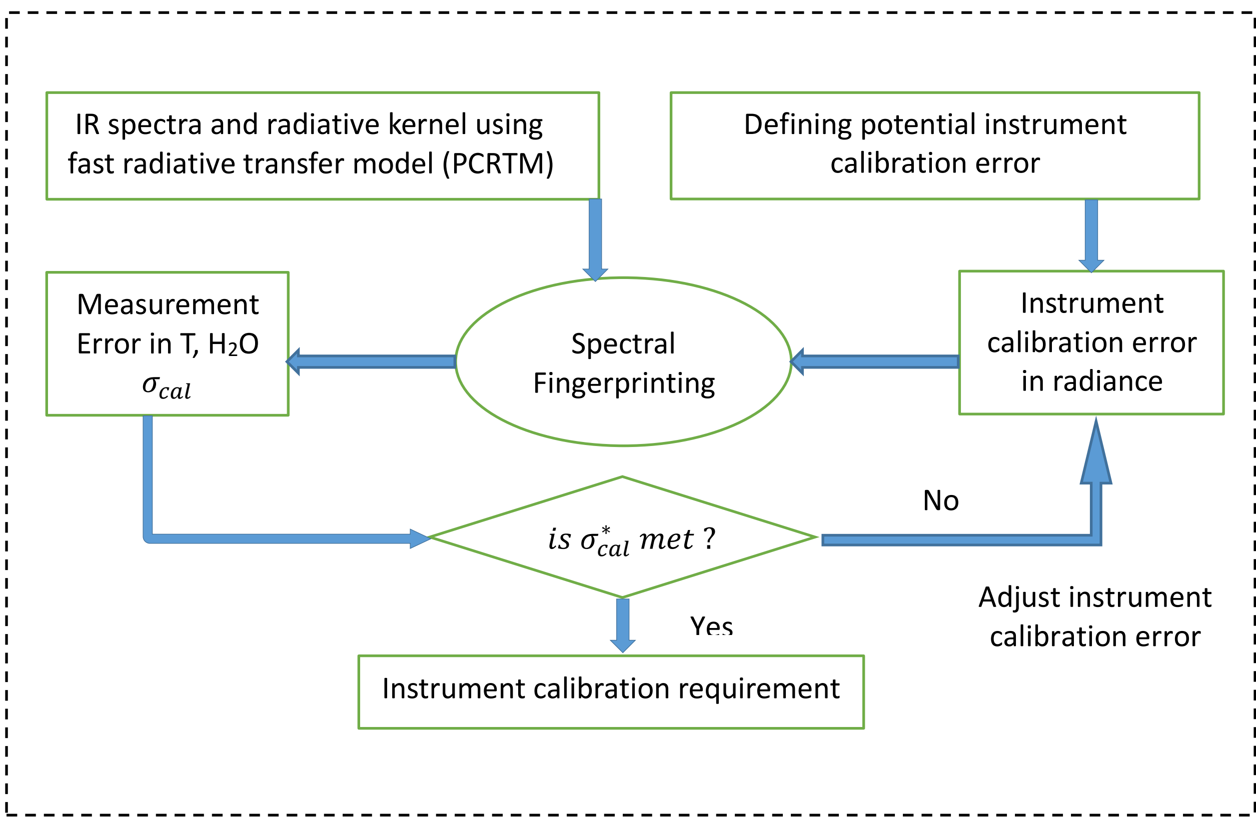

Fig. 1. Flow Diagram describing the procedures used in Section 2 and Section 3.

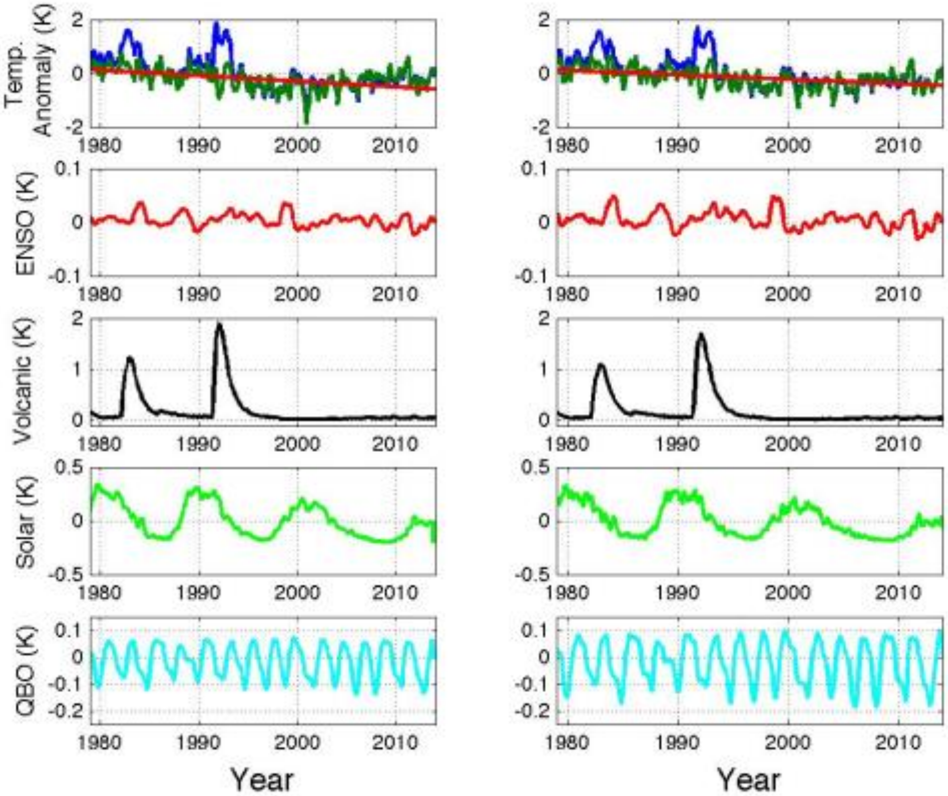

Fig. 2. Global air temperature anomaly at 70 hPa derived using MERRA (left column) and ERA Interim (right column) data. The subplots in the first row illustrate the temperature anomaly without accounting for ENSO, volcanic eruption, and solar cycle effects (blue curves), temperature anomaly after the subtraction of the volcanic eruption effect and the solar signals (dark green curves), and the derived linear trend (red lines) after the subtraction. Regression based estimations for ENSO (red curves), volcanic influence (black curves), solar signal (green curves), and QBO (cyan curves) are plotted in the second, the third, the fourth, and the fifth rows, respectively.

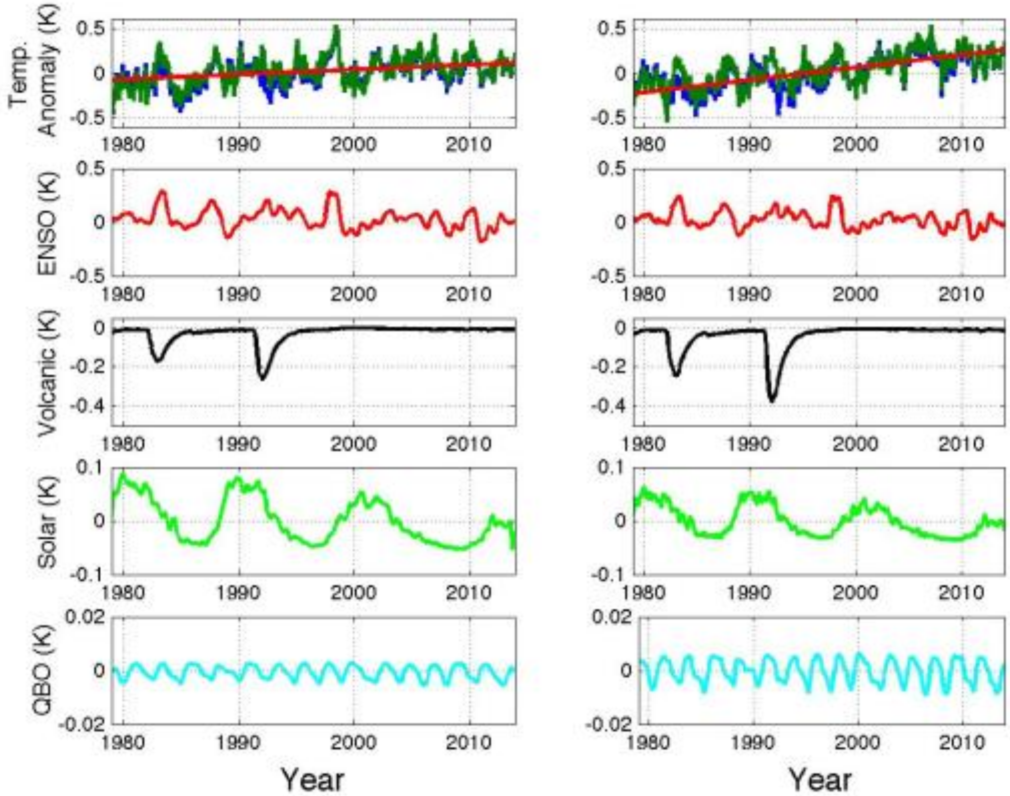

856 FIG. 3. Global air temperature anomaly at 975 hPa derived using MERRA (left column)
857 and ERA Interim (right column) data. See Figure 2 caption for more details.

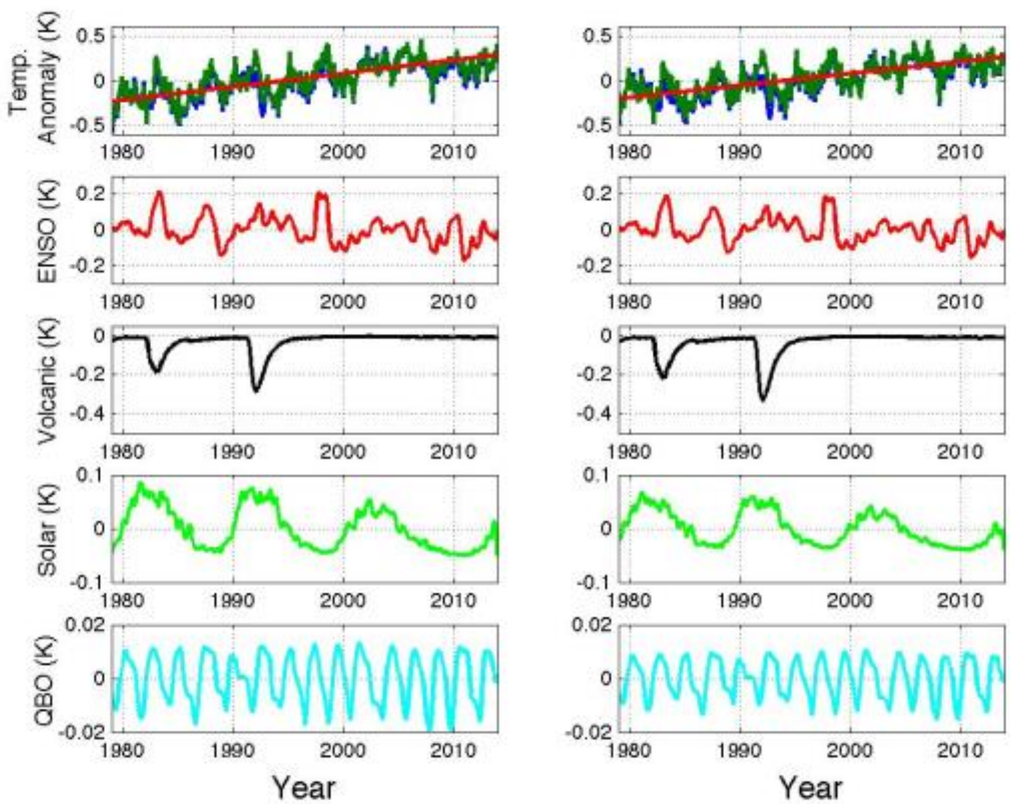

FIG. 4. Similar to Figure 3 but for the global surface skin temperature anomaly derived using MERRA (left column) and ERA Interim (right column) data. See Figure 3 caption for more details.

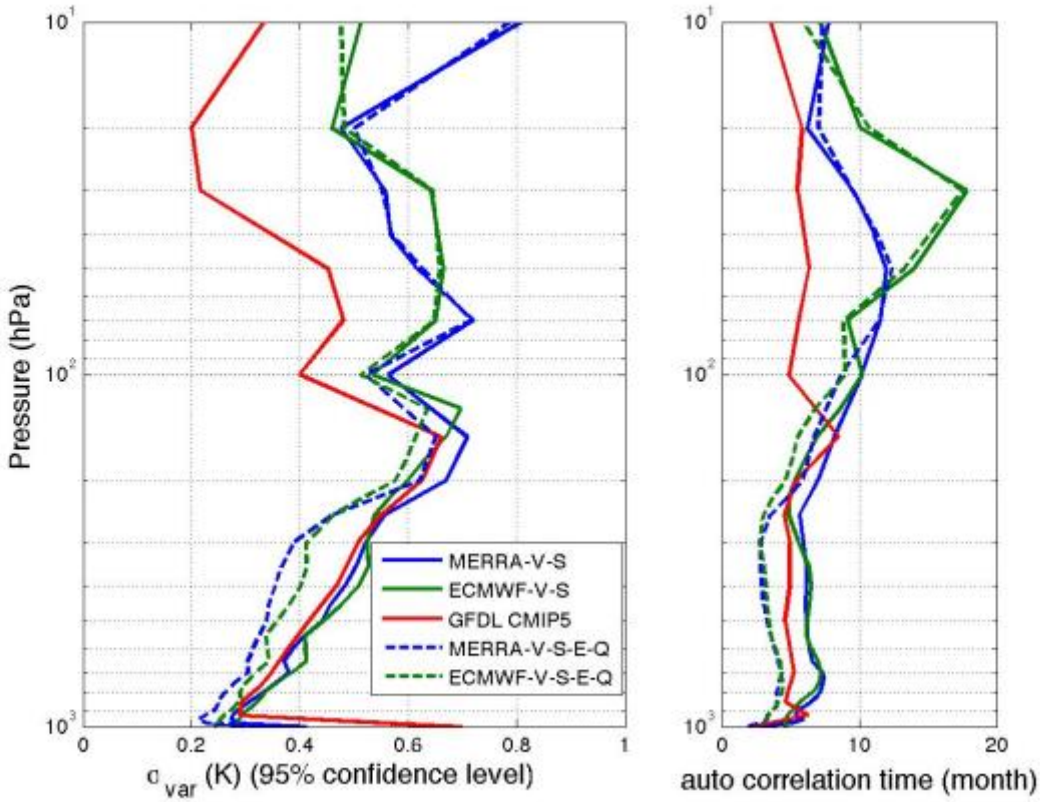

FIG. 5. Standard deviation of the temperature anomaly residual derived from MERRA, ECMWF reanalysis, and GFDL CM3 data. Left panel: Blue and green solid curves – standard deviation derived for MERRA and ECMWF reanalysis temperature anomaly free of volcanic and solar forcing; Red solid curve – variance of GFDL CM3 temperature; Blue and green dashed curves – standard deviation of MERRA and ECMWF obtained after subtracting the linear trend and all four major climate forcing influences. Right Panel: Corresponding autocorrelation time, τ_{var}, calculated using the first-order autoregressive (AR1) model. The legend for the curves on the right panel is the same as those shown on the left panel.

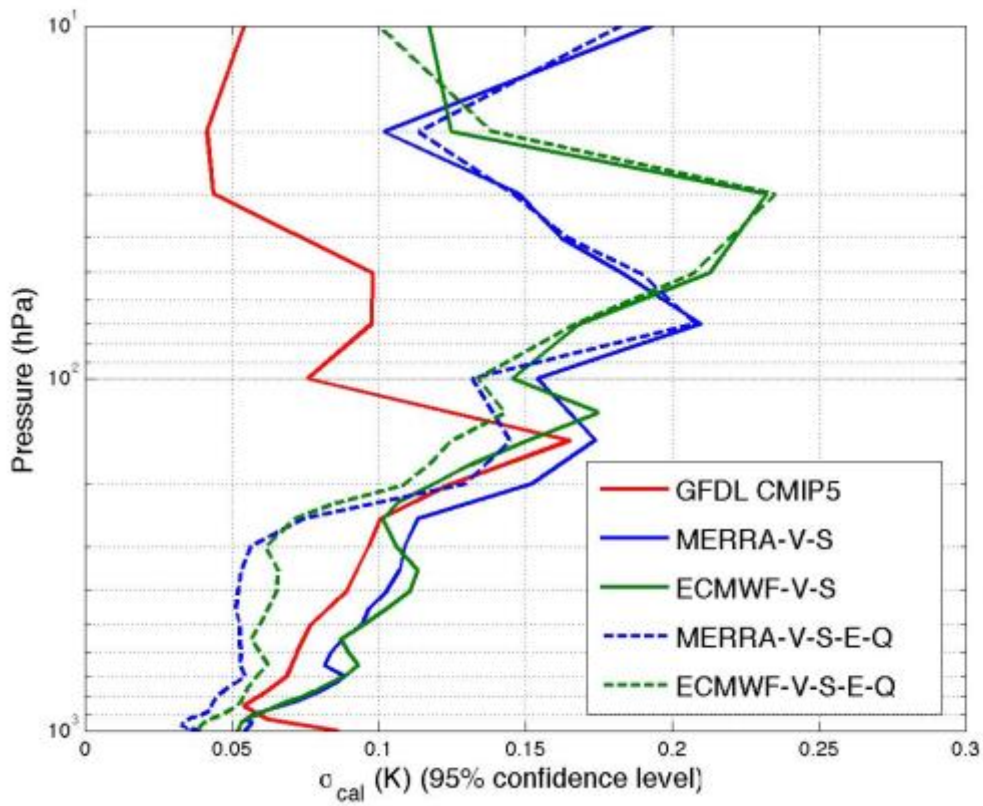

FIG. 6. Calibration requirement associated with the temperature variance and the autocorrelation time shown in Figure 5, given a trend accuracy uncertainty factor, U_a, of 1.2 and an instrument defined autocorrelation time, τ_{cal}, of 5 years.

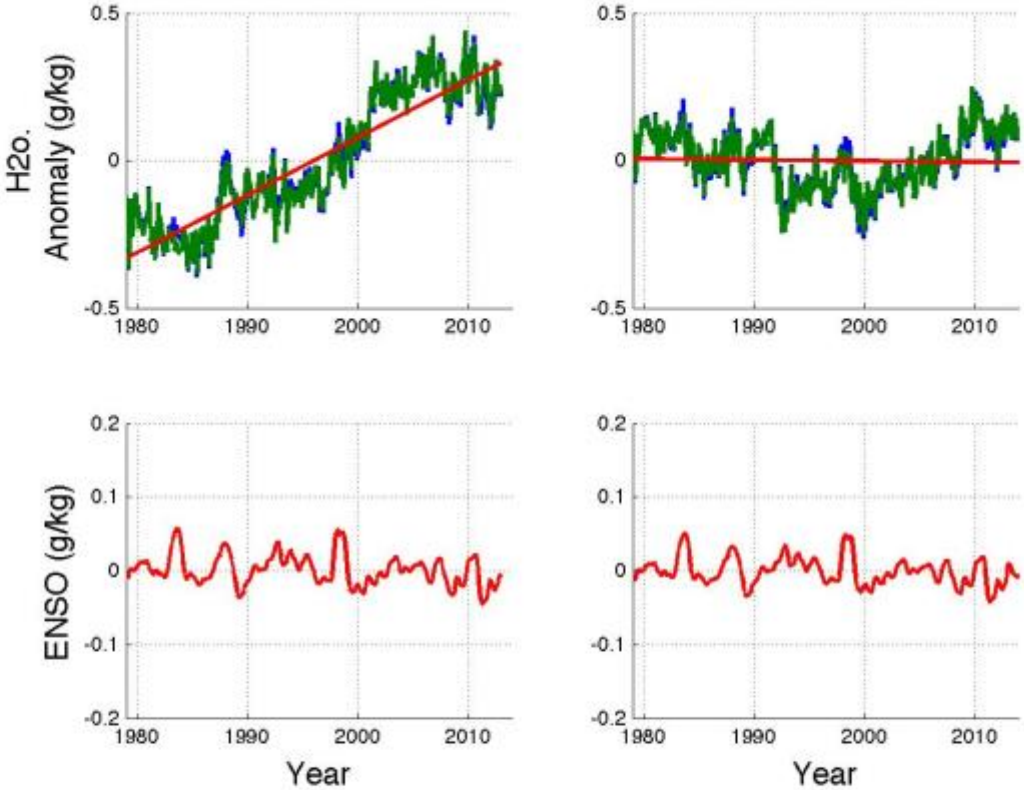

FIG 7. Global water vapor anomaly at 800 hPa derived using MERRA (left column) and ERA Interim (right column) data. The subplots in the top row illustrate the water vapor anomaly without accounting for ENSO effects (blue curves), water vapor anomaly after the subtraction of ENSO effects (dark green curves), and the derived linear trend (red lines) after the subtraction. Regression based estimations for ENSO (red curves) signals are plotted in the bottom row.

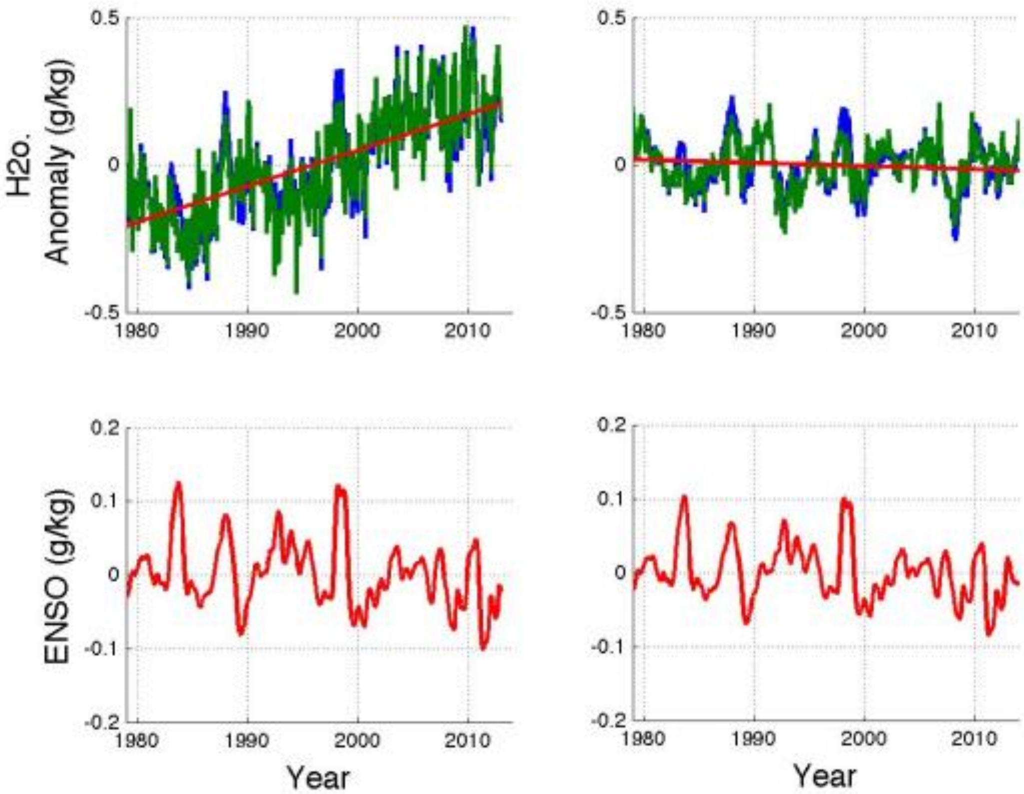

FIG. 8. Same as Figure 7 but for the global water vapor anomaly at 1000 hPa derived using MERRA (left column) and ERA Interim (right column) data.

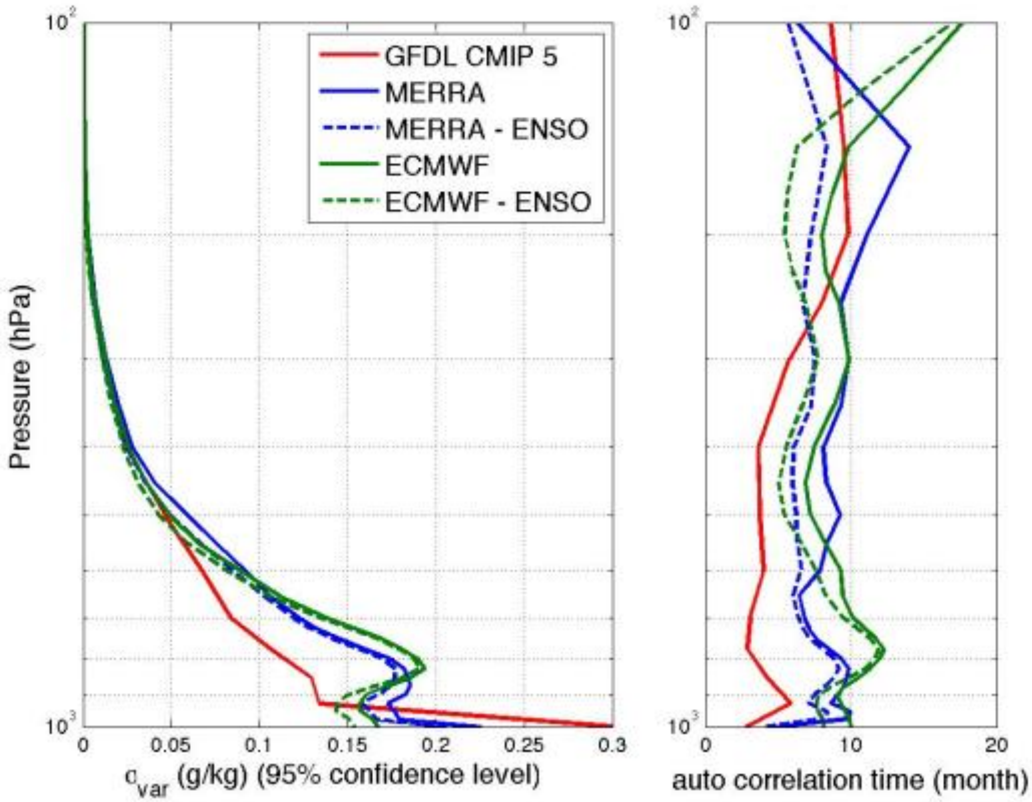

FIG. 9. Left panel: Standard deviation of the water vapor anomaly derived from the MERRA (blue curves) and the ECMWF reanalysis (green curves). Solid curves – standard deviation derived from the global average water vapor times series data. Dashed curves – standard deviation calculated after the subtraction of the ENSO signal. Red curve - standard deviation for GFDL water vapor. Right panel: corresponding lag 1 autocorrelation time.

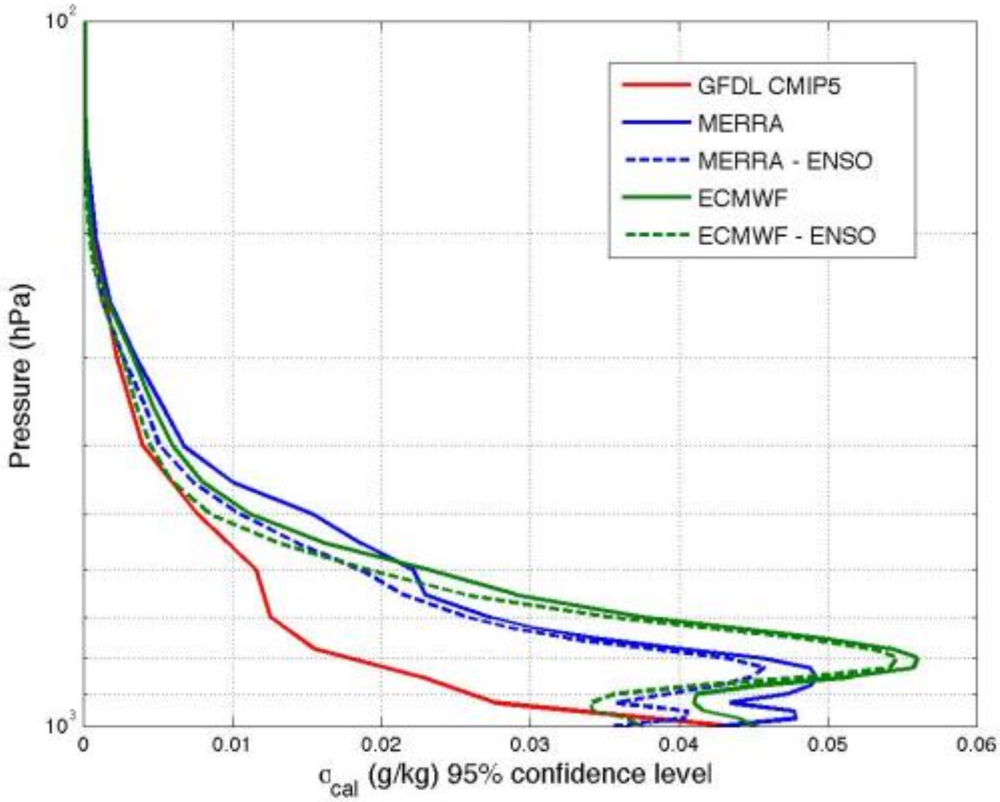

FIG. 10. Calibration requirement associated with the water vapor variance and the autocorrelation time shown in Figure 9, given a trend accuracy uncertainty factor U_a of 1.2 and an instrument defined autocorrelation time, τcal of 5 years.

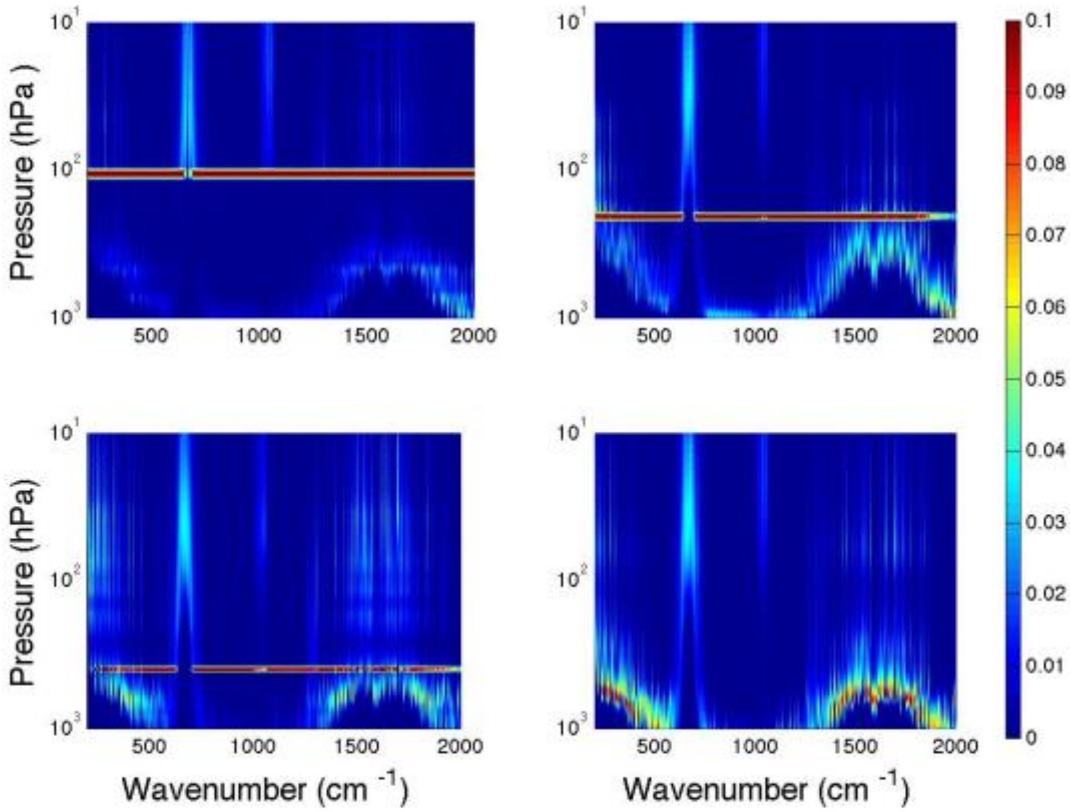

FIG. 11. Temperature Jacobian (dBT/dT, BT - Brightness Temperature, T – air temperature) plots under different sky conditions. Upper left: Ice cloud located at 106.6 hPa with a visible optical depth of 3.95. Upper right: Ice cloud located at 205.5 hPa with a visible optical depth of 2.21. Lower left: Water cloud located at 397.0 hPa with a visible optical depth of 1.36. Lower right: Clear sky.

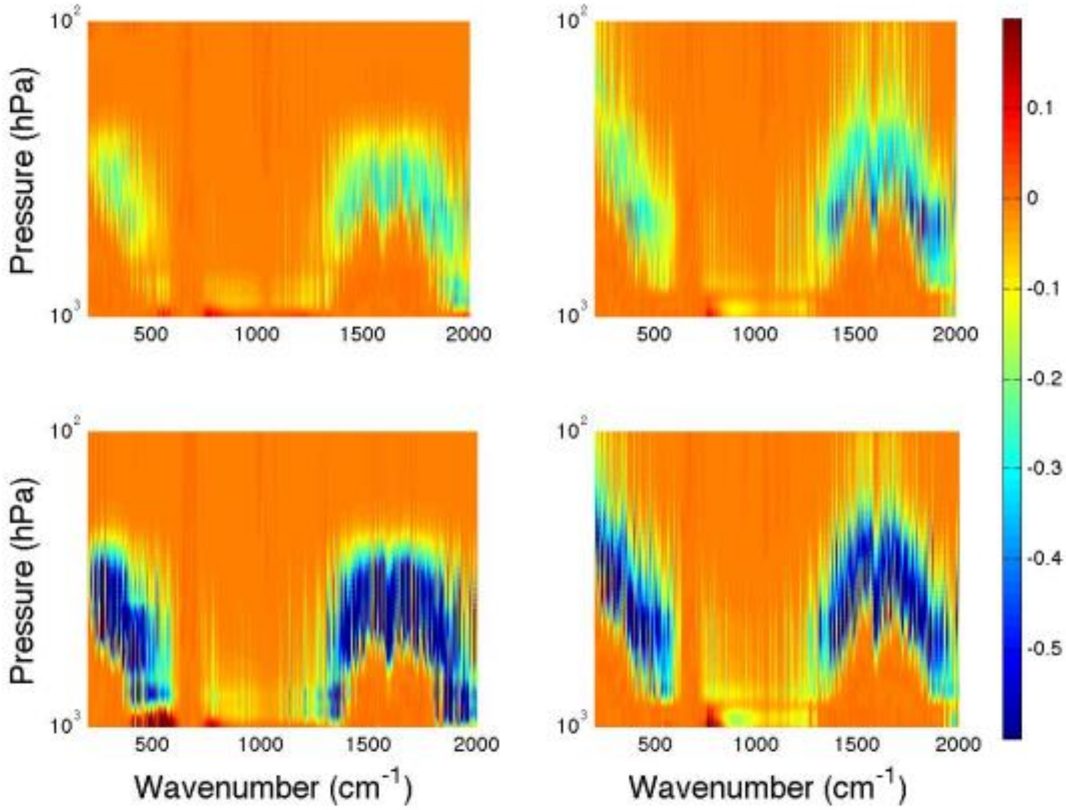

FIG. 12. Water vapor Jacobian (dBT/dlog(h2o)) plots under different sky conditions. Upper left: Ice cloud located at 106.6 hPa with a visible optical depth of 3.95. Upper right: Ice cloud located at 205.5 hPa with a visible optical depth of 2.21. Lower left: Water cloud located at 397.0 hPa with a visible optical depth of 1.36. Lower right: Clear sky.

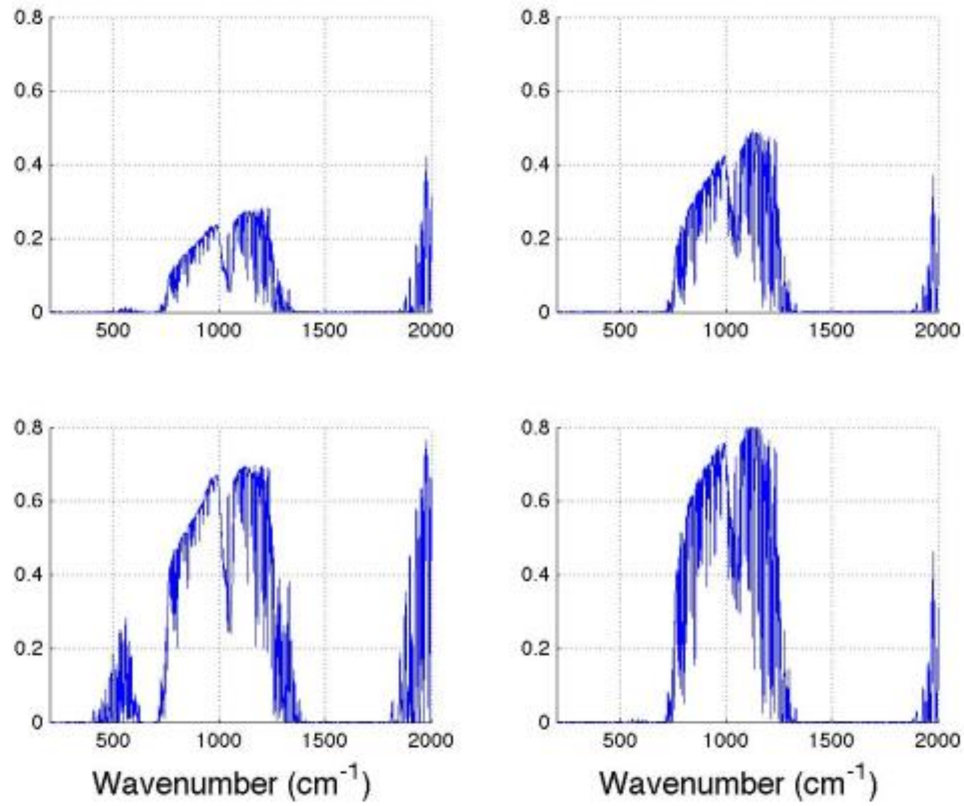

FIG. 13. Same as Figure 11 and 12 but showing sample Jacobian plots for surface skin temperature (dBT/dTskin).

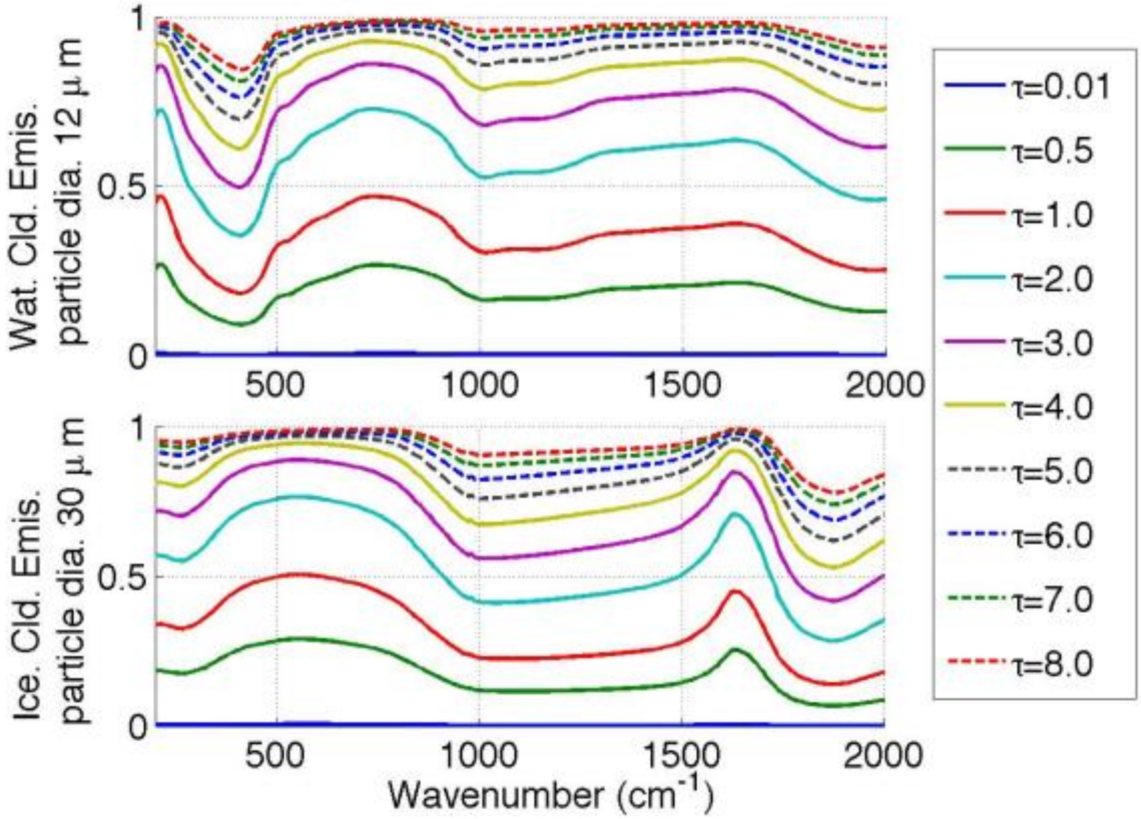

903 FIG. 14. Water and ice cloud emissivity in the CLARREO IR measurement band as
904 functions of cloud visible optical depth (at 500 nm wavelength), $\boldsymbol{\tau}$.

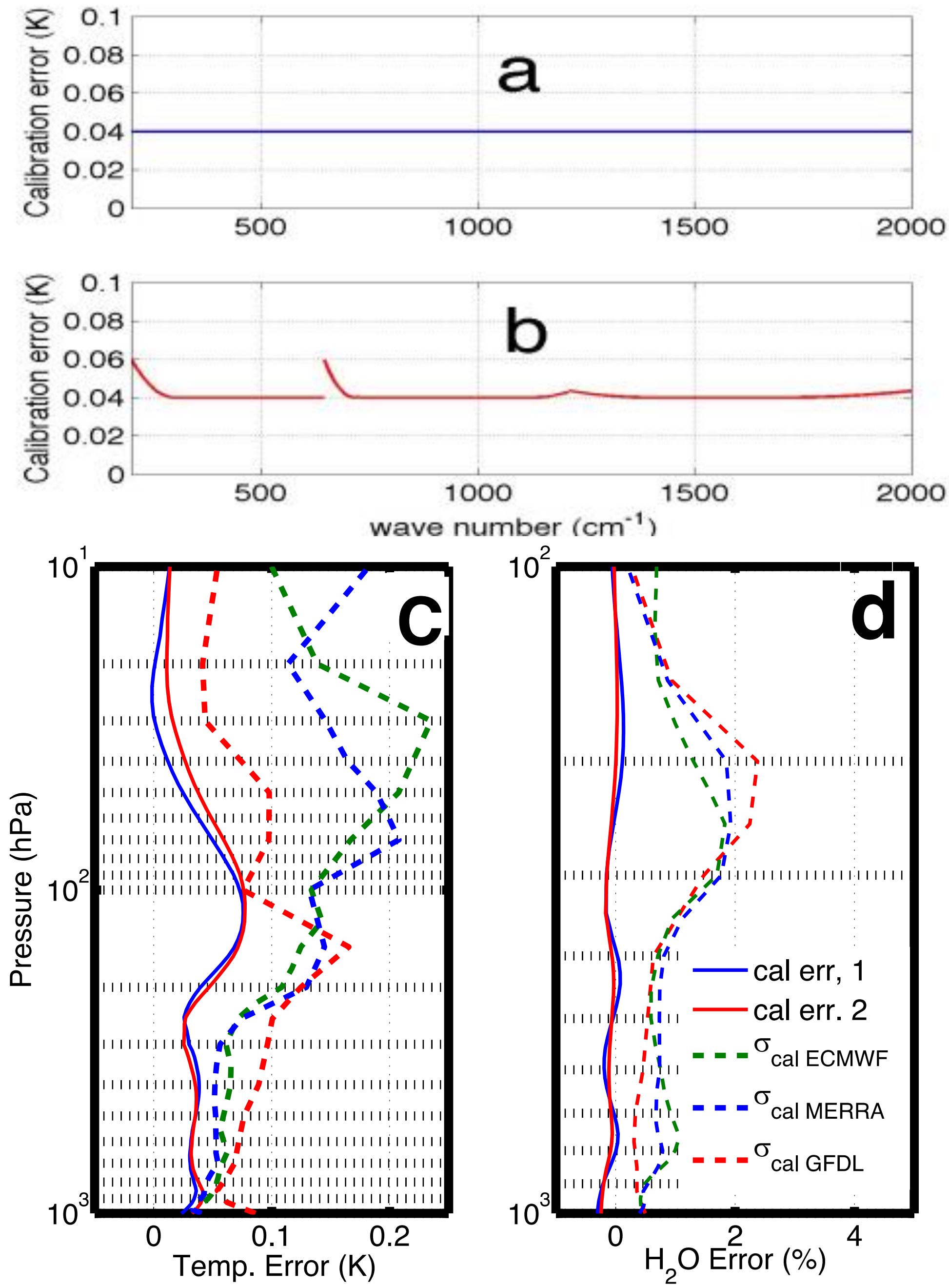

FIG. 15. The calibration errors and the corresponding errors introduced in temperature and water vapor observation. Upper panels: Spectral calibration error in brightness temperature (a. blue solid curve – 0.04 K (k=2) baseline error; b. red solid curve – potential calibration error based on a 0.04 K (k=2) baseline with detection band edge errors added); Lower panels: Corresponding calibration introduced temperature (c) and water vapor (d) fingerprinting errors (solid lines in matched colors). Calibration requirements for temperature and water vapor based on natural variability estimation results are plotted as dashed lines in lower panels as references: $\sigma_{cal\ ECMWF}$ –derived from ECMWF reanalysis data, $\sigma_{cal\ MERRA}$ – derived

from MERRA data, $\sigma_{cal\ GFDL}$ – derived from GFDL CM3 data. These calibration requirements are also plotted in Figs. 6 and 10.

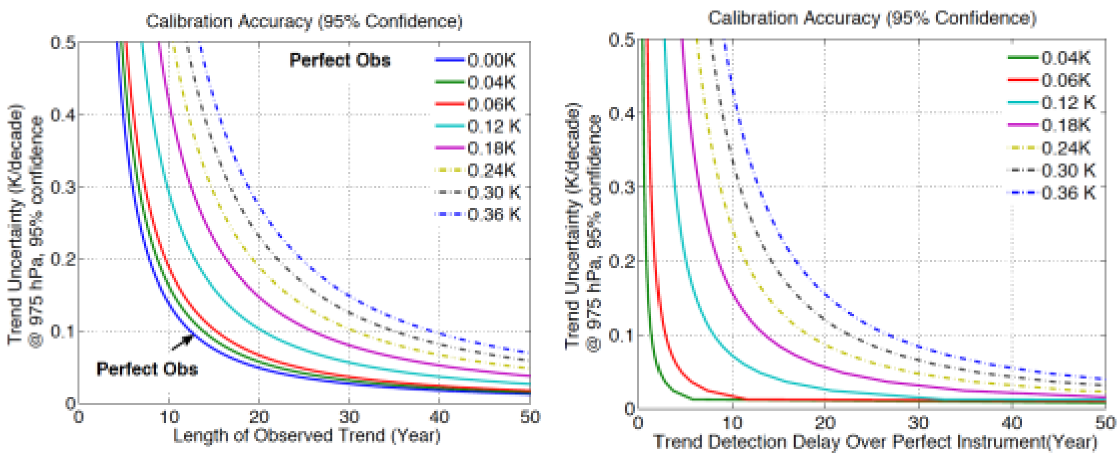

FIG. 16. Illustration of the dependence of the time to detect the low troposphere temperature trend on the observation systems' absolute calibration accuracy (95% confidence). The relationships calculated using the temperature natural variability values obtained when QBO and ENSO contributions are excluded from the natural variability: σ_{var} = 0.25 K, $\boldsymbol{\tau}_{\mathrm{var}}$ = 3.0 months (95% confidence).

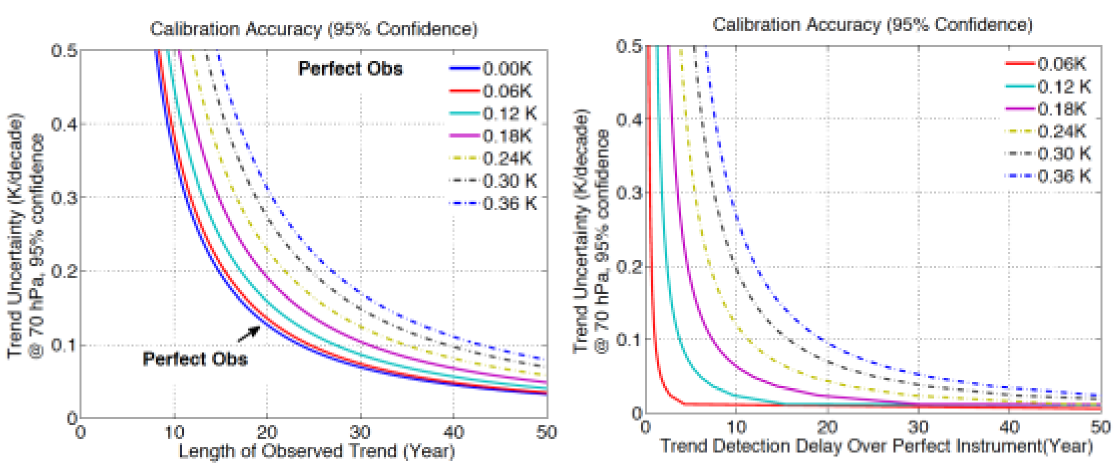

FIG. 17. Illustration of the dependence of the time to detect the stratospheric temperature (at 70 hPa with σ_{var} = 0.48 K, $\boldsymbol{\tau}_{\mathrm{var}}$ = 5.6 months (95% confidence)) cooling trend on the observation systems' calibration accuracy (95% confidence).

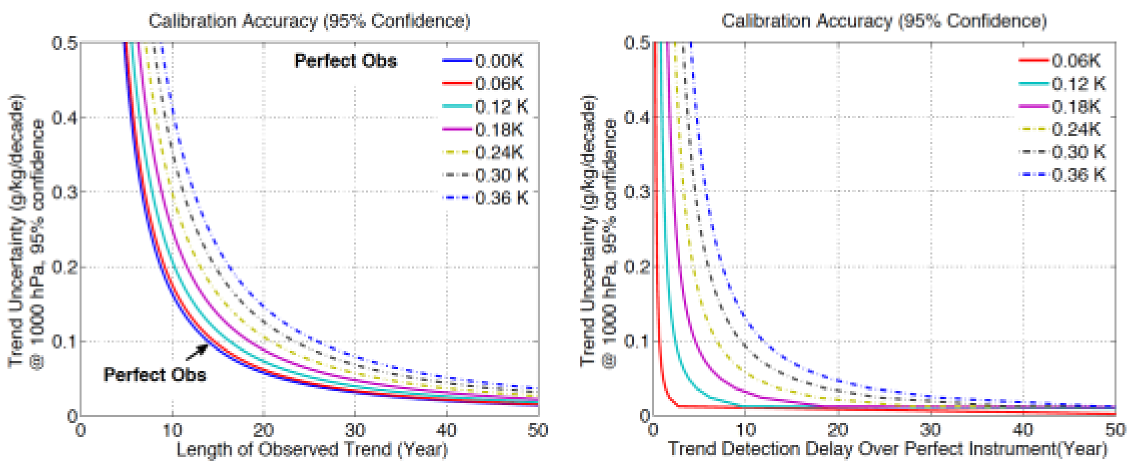

FIG. 18. Illustration of the dependence of the time to detect the specific surface humidity (at 1000 hPa with σ_{var} = 0.17 g/kg, τ_{var} = 9.6 months (95% confidence)) trend on the observation systems' calibration accuracy (95% confidence).